Faint absorption of the ground state hyperfine-splitting transitions of hydroxyl at 18 cm in the Galactic Disk[⋆]

M. R. Rugel[1, 2, 3, ⋆⋆], H. Beuther[4], J. D. Soler[5], P. Goldsmith[6], L. Anderson[7, 8, 9], A. Hafner[10], J. R. Dawson[11, 12], Y. Wang[4], S. Bihr[4], H. Wiesemeyer[3], R. Güsten[3], M.-Y. Lee[13, 14], D. Riquelme[3, 15], A. M. Jacob[3, 16], W.-J. Kim[16], M. Busch[17], S. Khan[3], and A. Brunthaler[3]

[1] National Radio Astronomy Observatory, PO Box O, 1003 Lopezville Road, Socorro, NM 87801, USA
[2] Center for Astrophysics | Harvard & Smithsonian, 60 Garden Street, Cambridge, MA 02138, USA
[3] Max Planck Institute for Radio Astronomy, Auf dem Hügel 69, 53121 Bonn, Germany
[4] Max Planck Institute for Astronomy, Königstuhl 17, 69117 Heidelberg, Germany
[5] Istituto di Astrofisica e Planetologia Spaziali (IAPS). INAF. Via Fosso del Cavaliere 100, 00133 Roma, Italy
[6] Jet Propulsion Laboratory, California Institute of Technology, 4800 Oak Grove Drive, Pasadena, 91109, USA
[7] Department of Physics and Astronomy, West Virginia University, Morgantown, WV 26506, USA
[8] Center for Gravitational Waves and Cosmology, West Virginia University, Chestnut Ridge Research Building, Morgantown, WV 26505, USA
[9] Adjunct Astronomer at the Green Bank Observatory, PO Box 2, Green Bank, WV 24944, USA
[10] School of Physics, The University of Sydney, Physics Rd, Camperdown NSW 2050, Australia
[11] School of Mathematical and Physical Sciences and Astrophysics and Space Technologies Research Centre, Macquarie University, 2109, NSW, Australia
[12] Australia Telescope National Facility, CSIRO Space & Astronomy, PO Box 76, Epping, NSW 1710, Australia
[13] Korea Astronomy and Space Science Institute, 776 Daedeok-daero, Daejeon 34055, Republic of Korea
[14] Department of Astronomy and Space Science, University of Science and Technology, 217 Gajeong-ro, Daejeon 34113, Republic of Korea
[15] Departamento de Astronomía, Universidad de la Serena, Raúl Bitrán 1305, la Serena, Chile
[16] I. Physikalisches Institut, Universität zu Köln, Zülpicher Str. 77, 50937 Köln, Germany
[17] Department of Astronomy & Astrophysics, University of California, San Diego, 9500 Gilman Drive, San Diego, CA 92093, USA

ABSTRACT

The interstellar hydride hydroxyl (OH) is a potential tracer of CO-dark molecular gas. We present new high-sensitivity absorption line observations of the four ground state hyperfine-splitting transitions of OH at 18-cm wavelength towards four Galactic and extra-galactic continuum sources as follow-up to the THOR survey. We compare these to deep observations of the [C II] 158 μm line at 1.9 THz obtained with the upGREAT instrument on SOFIA, observations of the neutral atomic hydrogen (H I) 21 cm line with the VLA, and CO ($J = 2$–1) lines obtained with the APEX PI230 receiver at the APEX 12 m sub-mm telescope. We trace OH over a large range of molecular hydrogen column densities of 7.9×10^{19} cm^{-2} to 4.7×10^{22} cm^{-2}, and derive OH abundances with respect to molecular and total hydrogen column densities of $X_{\mathrm{OH,H_2}} = N_{\mathrm{OH}}/N_{\mathrm{H_2}} = 1.2^{+0.3}_{-0.2} \times 10^{-7}$ and $X_{\mathrm{OH,H}} = N_{\mathrm{OH}}/N_{\mathrm{H}} = 4.8^{+0.9}_{-0.8} \times 10^{-8}$, respectively. Increased sensitivity and spectral resolution allowed us to detect weak and narrow features with the lowest column density detected at $N_{\mathrm{OH}} = 3.7 \times 10^{13}$ cm^{-2}. The increase in sensitivity is a factor of 5 in direct comparison at the resolution the OH observations in the THOR survey (1.5 km s^{-1}). We identify only one OH absorption component out of 23 without CO counterpart, yet several with intermediate molecular gas fractions (f$_{\mathrm{mol}} \leq 0.8$). A potential association of [C II] 158 μm emission with an OH absorption component is seen toward one sightline. Our results confirm that OH absorption traces molecular gas across diffuse and dense environments of the interstellar medium. At the sensitivity limits of the present observations our detection of only one CO-dark molecular gas feature appears in agreement with previous studies. We conclude that if OH absorption was to be used as a CO-dark molecular gas tracer, deeper observations or stronger background targets are necessary to unveil its full potential as a CO-dark molecular gas tracer, and yet it will never be an exclusive tracer of CO-dark molecular gas. For OH hyperfine-splitting transitions in the vicinity of photodissociation regions in W43-South, we detect a spectral and spatial offset between the peak of the inversion of the OH 1612 MHz line and the absorption of the OH 1720 MHz line on the one hand, and the absorption of the OH main lines on the other hand, which provides additional constraints on the interpretation of the OH 18 cm line signatures typical of HII regions.
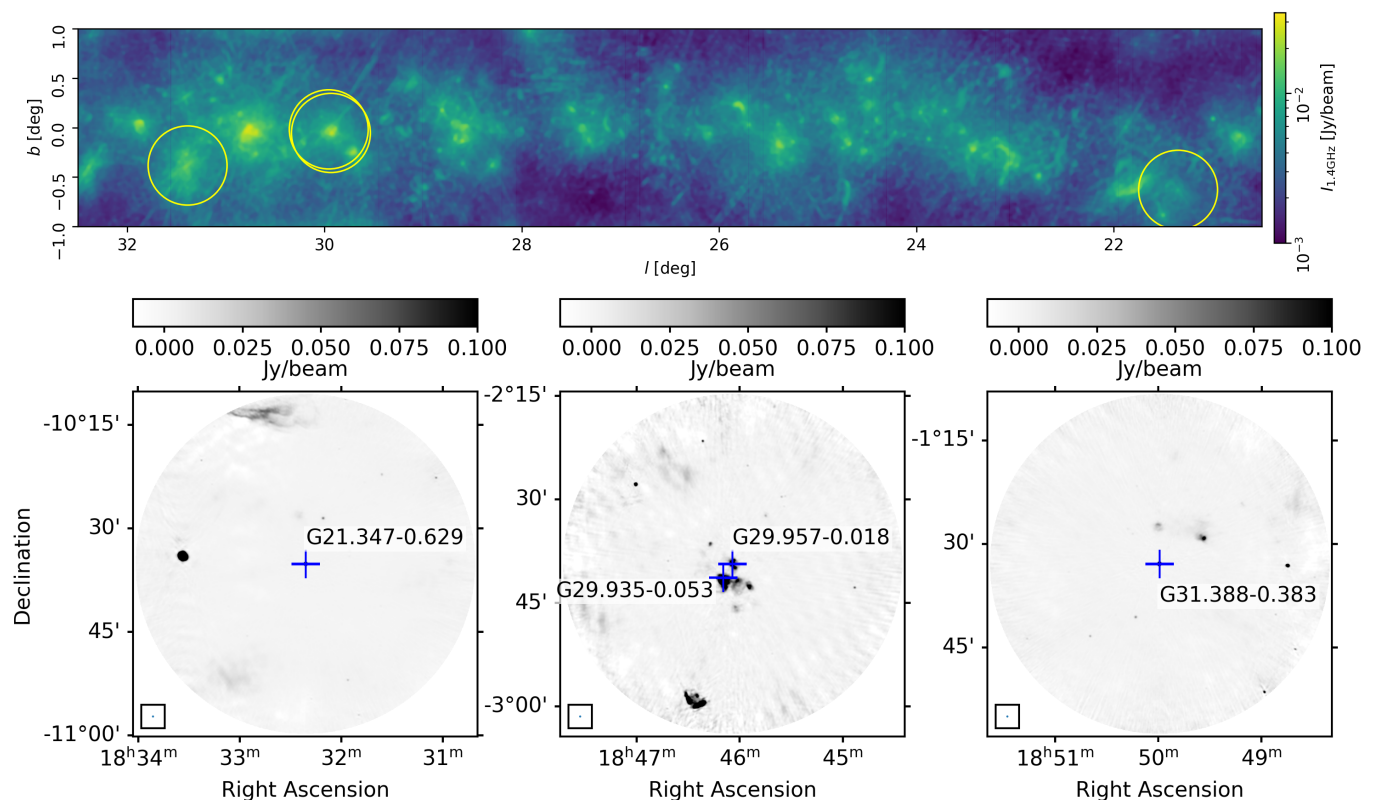
Key words. ISM: clouds – ISM: abundances – radio lines: ISM – surveys – molecular data – instrumentation: interferometers

1. Introduction

Molecular clouds are the birthplaces of stars. They form out of the diffuse atomic interstellar medium (ISM) once sufficient

Fig. 1. *Top:* THOR 1.4 GHz continuum emission in the Galactic coordinate frame (Wang et al. 2020). The sources discussed here are located at the center of the yellow circles. *Bottom:* VLA 1.4 GHz continuum towards the four positions analyzed in this work *(blue crosses)* in equatorial coordinates. The images are smoothed to an angular resolution of 18″.

shielding from the interstellar radiation field is provided (e.g., Dobbs et al. 2014; Chevance et al. 2023; Pineda et al. 2023, and references therein), which also enables star formation (Glover & Clark 2012). It is essential to study the formation of molecular clouds for our understanding of star formation in the Milky Way.

Gas in cold molecular clouds consists mostly of H_2. H_2 emission from molecular clouds can be detected in shocks (e.g., Beckwith et al. 1983; Beuther et al. 2023, see also discussion in Sternberg 1989a) or by fluorescence emission (e.g., Sellgren 1986; Witt et al. 1989; Sternberg 1989b; Burkhart et al. 2025). Its rotational transitions with excitation energies about 500 K are impossible to be observed in emission under cold ISM conditions. Alternatively, such clouds are commonly studied with observations of the CO molecule (Wilson et al. 1970), whose low angular momentum (J) rotational lines are easily accessible at millimeter wavelengths. Several studies have indicated the presence of molecular gas not traced by CO emission (e.g., Grenier et al. 2005; Wolfire et al. 2010; Smith et al. 2014; Planck Collaboration et al. 2011). CO-dark molecular hydrogen gas, here defined as gas without detection of ^{12}CO emission, has been found across the Galaxy at significant fractions (Pineda et al. 2013; Langer et al. 2014; Busch et al. 2021), in particular in regions of low extinction (Paradis et al. 2012; Xu et al. 2016; Remy et al. 2018). Observationally constraining the properties of "CO-dark" gas or simply "dark" gas thus contributes to our understanding of both the H I-to-H_2 conversion, as well as the onset of molecular cloud and star formation.

The ground state hyperfine-splitting (HFS) transitions of the hydroxyl molecule (OH) at cm wavelengths have been detected in regions with CO-dark gas. Xu et al. (2016) have investigated

the relation between OH emission and dark gas fractions across the molecular cloud boundary in Taurus. Allen et al. (2015), Busch et al. (2019) and Busch et al. (2021) detected OH emission towards CO-dark lines-of-sight in the outer Galaxy, and Li et al. (2018) found OH absorption components without CO counterparts towards strong extragalactic continuum sources at high Galactic latitudes. Other detailed Galactic plane surveys investigating OH in emission across the Galactic plane include The Southern Parkes Large-Area Survey in Hydroxyl (SPLASH; Dawson et al. 2022). OH has also been found in high-mass star forming regions in association with photon-dominated/photo-dissociation regions (PDRs) and outflows (e.g., Goicoechea et al. 2011; Wampfler et al. 2011, 2013). The abundance of OH has been analyzed in several studies using the 18 cm lines (e.g., Goss 1968; Crutcher 1979; Liszt & Lucas 1996, 2002), with a detailed, recent studies of OH absorption presented in Hafner et al. (2023) and Nguyen et al. (2018). The OH abundance was also investigated with the fundamental OH rotational transitions into the ground state at far-infrared wavelengths (Wiesemeyer et al. 2016; Jacob et al. 2022), as well as through its electronic transition at ultra-violet wavelengths (e.g. Weselak et al. 2010). Given that the OH hyperfine splitting transitions at 18-cm are readily accessible at ever higher resolution and sensitivity by today's and future radio telescopes, a detailed study of OH in different Galactic environments seems warranted.

In this work, we present deep OH absorption observations along the lines of sight towards three bright background sources, as a follow-up study to The H I, OH, Recombination Line survey (THOR; Beuther et al. 2016; Wang et al. 2020), which observed the OH 18 cm lines over a large fraction of the first Galactic

quadrant (Rugel et al. 2018; Beuther et al. 2019). We discuss the OH absorption towards four continuum sources which are chosen to be strong enough to reveal faint OH absorption from diffuse sightline clouds with typical optical depths of $\tau < 0.1$ (e.g., Dickey et al. 1981; Liszt & Lucas 1996), and increased spectral resolution as compared to THOR to resolve narrow absorption features. The field of view of one of the targets includes an extended H ii region complex, which enables additional studies of OH in PDRs (e.g., Brogan & Troland 2001) towards H ii regions.

Furthermore, we search for associated [C ii] emission using observations carried out with the Stratospheric Observatory for Far-Infrared Astronomy (SOFIA; Young et al. 2012). [C ii] emission can originate from different ISM environments, including the transition region between atomic and molecular gas. It has been used to estimate the CO-dark gas fraction in individual clouds (Xu et al. 2016), as well over the entire Milky Way disk (Pineda et al. 2013). [C ii] emission has been directly detected in the diffuse ISM (Goldsmith et al. 2018), and may trace gas accretion onto molecular clouds (Heyer et al. 2022). [C ii] is readily detected in absorption along the line-of-sight in clouds of varying molecular gas fractions (e.g., Gerin et al. 2015; Jacob et al. 2022).

The goal of this work is to characterize the abundance of the OH molecule in different ISM conditions. Of particular interest are the properties of the OH gas in diffuse ISM environments where CO becomes a less-reliable tracer of the bulk molecular hydrogen content. We will present comparisons between [C ii] emission and OH absorption. We additionally report findings on the excitation conditions of OH in H ii regions.

2. Observations

2.1. VLA observations

We selected four continuum sources with a flux of ~ 1 Jy beam^{-1} (Table 1). The H ii region G29.957−0.018 has a spectral index[1] of $\alpha = 0.9$ (Wang et al. 2018), where positive spectral indices indicate thermal emission. G29.957−0.018 and G29.935−0.053 are part of the H ii region complex W43-South, which has been attributed to the W43 complex (Motte et al. 2014). The continuum emission in W43-South at cm wavelengths has presented in Beltrán et al. (2013), and the entire W43 complex is located at a distance of 5.49 kpc (Zhang et al. 2014). Two sources are of extragalactic origin (G21.347−0.629 and G31.388−0.383; with $\alpha = 0.0$ and $\alpha = -0.9$). All sources were selected based on OH absorption components in the THOR survey (Rugel et al. 2018) with weak (G29.957−0.018) or no (G31.388−0.383) ^{13}CO (1−0) emission counterparts in the Galactic Ring Survey (GRS; Jackson et al. 2006).

We chose a channel width of 0.488 kHz (0.1 km s^{-1} at 1420 MHz), which is a significant improvement in comparison to the THOR survey (1.5 km s^{-1}; Rugel et al. 2018). The bandwidth is 4 MHz for the H i and OH 1665/1667 MHz bands, and 2 MHz bands for the OH 1612 and OH 1720 MHz lines, which results in at least 300 km s^{-1} of usable bandwidth for the OH transitions (see Table 2 for frequencies discussed in this work). We observed for 8 nights between June and August 2017 with the VLA in C-configuration, with a total integration time of 7 h for G21.347−0.629, 4 h for G29.957−0.018 and G29.935−0.053, and 3 h for G31.388−0.383. The observations were split into

blocks of 2 hours. We observed 3C286 for 10-20 minutes for bandpass calibration and used J1822-0938 as a complex gain calibrator.

We processed the observational data with the CASA[2] calibration pipeline. We inspected the data for antenna and baseline artifacts. The calibrated data were imaged and de-convolved using the CASA task `clean`. We subtracted the continuum from line-free channels before imaging, and imaged spectral line cubes and continuum emission separately. The restoring beam is between 17″2×12″8 and 12″8×11″5. We smoothed all data to 18″ resolution (full width at half maximum, FWHM). The noise in a 0.2 km s^{-1}-wide channel is between 5–7 mJy beam^{-1} for the OH transitions. The increase in sensitivity is a factor of 5 in direct comparison at the resolution the OH observations in the THOR survey (10 mJy beam^{-1} at 1.5 km s^{-1} spectral resolution). For the H i line, the sensitivity is around 5 mJy beam^{-1} in a 0.5 km s^{-1}-wide channel, corresponding to a brightness temperature of ∼10 K. At velocities of Galactic H i emission, the noise increases up to a factor of two due to significant contributions of the H i emission to the system temperature.

2.2. SOFIA [CII] observations

We used the upGREAT receiver on the SOFIA telescope (Risacher et al. 2016) to measure the [C ii] 158 μm line (see Table 2) towards G29.935−0.053 and G31.388−0.383. Due to observing time constraints, we were unable to obtain observations towards G21.347−0.629 and G29.957−0.018 was restricted to guaranteed time programs at the time of the proposal. The observations were conducted on June 8, 13, 19 and 20 of 2018 during flights from Christchurch, New Zealand, at an altitude of about 13 km as part of the project 06_0171 in position-switching total power mode. We used the standard SOFIA GREAT data reduction pipeline kalibrate. The spectra were corrected for atmospheric absorption.

The SOFIA upGREAT instrument consists of an array of 7 receivers ("pixels") which observe simultaneously and and comprises two frequency channels operating at 1.9 THz and 4.7 THz, respectively. The low-frequency array was tuned to 1.9 THz to cover the [C ii] 158 μm line, with an angular resolution of 14″1. The high-frequency array was tuned to 4.7 THz to cover the [O i] 63 μm line (see Table 2), with an angular resolution of 6″3. The data were calibrated with a forward efficiency of η_f=0.97 and a main-beam efficiency which varies among the pixels between 0.55 and 0.70. As [C ii] 158 μm emission extends to high Galactic latitudes, we chose two separate reference positions for both sources, identified as regions with low CO emission and low dust opacity using data from the Planck mission (Planck Collaboration et al. 2011, 2014) in absence of large scale maps of [C ii] 158 μm emission. The time on each source was equally shared between the on-target position (50 %) and two reference positions (25 % each).

Pixel 2 was only available in vertical polarization, while all other pixels were observed in both linear polarizations. We note that pixel 4 shows higher baseline instabilities. Overall baselines are subtracted with first-order polynomials. For each pixel, we averaged all polarizations and observations with different reference positions. Similar steps have been applied for the [O i] 63 μm line, for which only the vertical polarization orientation was available. In the end, we averaged all available polarizations and spectra obtained with different reference positions. The final RMS on main beam temperature scales in the central pixel is

---

[1] The spectral index is defined as $S_\nu = S_0 \times \left(\frac{\nu}{\nu_0}\right)^\alpha$, where S_0 is the flux at a reference frequency, ν_0 at 1.4 GHz

[2] http://casa.nrao.edu; version 4.7.2; pipeline version 1.3.11

Table 1. Target locations and 1.4 GHz continuum fluxes

Source	l	b	R. A. (J2000)	Dec. (J2000)	$F_{\text{cont,peak}}$(1.4 GHz at 18″)
	°	°	(h m s)	(° m s)	[Jy beam^{-1}]
G21.347−0.629	21.347	−0.629	18 32 20.9	−10 35 11.4	0.9
G29.957−0.018	29.957	−0.018	18 46 04.2	−02 39 19.3	1.0
G29.935−0.053	29.935	−0.054	18 46 09.6	−02 41 27.5	0.4
G31.388−0.383	31.388	−0.383	18 49 59.2	−01 32 56.0	1.3

$\sigma(T_{\text{mb}}) \sim 0.1$ K in a 0.39 km s^{-1} channel for the [C II] 158 μm, and ~ 0.2 K in a 0.15 km s^{-1} channel for the [O I] 63 μm spectra. Residual baseline ripples are present in both lines at a low level. We flag any remaining channels with potential contamination from emission in the reference position, and disregard them in the following analysis. All SOFIA upGREAT spectra are shown in Appendix B.

For G29.935−0.053, we searched for the [^{13}C II] line. While we see indications of the $F=1$–0 line, the $F=0$–1 line is blended with the [C II] 158 μm line, and the $F=1$–1 line remains undetected. The velocity of the faint [^{13}C II] $F=1$–0 line aligns with the velocity of a potential [C II] 158 μm self-absorption dip in many of the pixels. Due to overlap in velocity with the complex [C II] 158 μm emission along the line of sight across the Galaxy, a clear identification of the [^{13}C II] $F=1$–0 remains difficult.

2.3. CO observations with the APEX telescope and from archival data

We observed the $J=2$–1 lines of different isotopologues of the CO molecule with the PI230 instrument on the Atacama Pathfinder EXperiment (APEX) 12 m submillimeter telescope (Güsten et al. 2006) for the sources for which we had obtained SOFIA [C II] 158 μm observations, G31.388−0.383 and G29.935−0.053. We observed both sources in position-switching mode. The tuning frequencies were chosen to cover the ^{12}CO, ^{13}CO, and C^{18}O isotopologues, as well as the H30α radio recombination line. The CO lines have been resampled to a spectral resolution of 0.2 km s^{-1}. The T_{mb} sensitivity is 0.04 K. To probe similar scales among different isotopologues, the observations were convolved to an angular resolution of 31″ (FWHM) from a resolution of 27″.1 for ^{12}CO(2–1) and 28″.4 for ^{13}CO (2–1) and C^{18}O (2–1), respectively.

For G21.347−0.629 and G29.957−0.018, we used archival CO observations from three surveys. ^{13}CO(1–0) observations are obtained from the GRS survey (Jackson et al. 2006). The GRS survey maps have a half-power beam width of 46″, and we correct all data for a main-beam efficiency of $\eta_{\text{mb}} = 0.48$. Also, we used maps of ^{12}CO(1–0) and C^{18}O(1–0) emission from the FOREST Unbiased Galactic plane Imaging survey with the Nobeyama 45-m telescope (FUGIN) at 0.65 km s^{-1} spectral resolution (Umemoto et al. 2017), after convolving them from their original angular resolution of 20″ (FWHM) to 46″.

3. Analysis

3.1. OH and H I column densities

We determined the column density of OH from the 1667 MHz line, as its optical depth tends to be higher than the 1665 MHz line, thus likely being detected at a better signal-to-noise for a given excitation temperature. We estimated the optical depth of the H I and OH lines using $\frac{F_{\text{line}}}{F_{\text{cont}}} = e^{-\tau}$, with F_{line} corresponding to the flux density of the spectral line without continuum subtraction,

Table 2. Spectral lines discussed in this work.

Line	Frequency [GHz]
OH $^2\Pi_{3/2}$ ($J=3$–2, $F=1^+$–2^-)	1.612231
OH $^2\Pi_{3/2}$ ($J=3$–2, $F=1^+$–1^-)	1.665402
OH $^2\Pi_{3/2}$ ($J=3$–2, $F=2^+$–2^-)	1.667359
OH $^2\Pi_{3/2}$ ($J=3$–2, $F=2^+$–1^-)	1.720530
H I (^{2}S$_{1/2}$, $F=1$–0)	1.420406
^{12}CO ($J=1$–0)	115.2712
^{12}CO ($J=2$–1)	230.5380
^{13}CO ($J=1$–0	110.2013
^{13}CO ($J=2$–1)	220.3987
C^{18}O ($J=1$–0	109.7822
C^{18}O ($J=2$–1)	219.5604
[C II] (^{2}P$_{3/2}$–^{2}P$_{1/2}$)	1900.537
[O I] 63 μm (^{3}P$_1$–^{3}P$_2$)	4744.777
[^{13}C II] (^{2}P$_{3/2}$–^{2}P$_{1/2}$, $F=1$–1)	1900.136
[^{13}C II] (^{2}P$_{3/2}$–^{2}P$_{1/2}$, $F=2$–1)	1900.466
[^{13}C II] (^{2}P$_{3/2}$–^{2}P$_{1/2}$, $F=1$–0)	1900.950

F_{cont} the continuum flux density and τ the optical depth. The continuum was derived from the absorption-free channels. Given the strong continuum, we assumed that H I and OH emission is a negligible contribution to the spectrum after filtering extended emission with the interferometer. For saturated H I absorption channels, we calculate a lower limit on the optical depth by assuming a minimum H I absorption depth at the 3-σ noise level.

The OH excitation temperature is typically within a few Kelvin of the cosmic microwave background temperature (Li et al. 2018; Hafner et al. 2023), with a distribution up to higher values found up to $T_{\text{ex}} = 20$ K. We fix the excitation temperature at $T_{\text{ex}} = 5$ K and account for an uncertainty of a factor of two for the excitation temperature in the error analysis. The OH column density is then calculated as:

$$\frac{N_{\text{OH}}}{T_{\text{ex}}} = \frac{C_0}{f} \int \tau \, dv, \tag{1}$$

where N_{OH} describes the total OH column density in particles cm^{-2} integrated over the optical depth profile in velocity, T_{ex} is the excitation temperature in Kelvin, and the pre-factors are given as $C_0 = 4.0 \times 10^{14}$ cm^{-2} K^{-1}km^{-1}s for the 1665 MHz line and $C_0 = 2.24 \times 10^{14}$ cm^{-2} K^{-1}km^{-1}s for the 1667 MHz line (e.g., Goss 1968; Turner & Heiles 1971; Stanimirović et al. 2003, calculated using Einstein coefficients from Turner 1966). For the filling factor we assumed $f = 1$.

Similarly, we derive the H I column densities using

$$N_{\text{H I}} = 1.8224 \times 10^{18} \frac{T_{\text{spin}}}{\text{K}} \int \tau(\text{v}) \left(\frac{d\text{v}}{\text{km s}^{-1}}\right) \text{cm}^{-2}. \tag{2}$$

We assume an average spin temperature of the absorbing H I gas of $T_{\text{spin}} = 100$ K, as the absorption is dominated by the cold neutral medium. We estimated the uncertainties in this assumption

to be about a factor of two, given the significant spread in the distribution found in previous studies (e.g., Heiles & Troland 2003; Murray et al. 2018; Dickey et al. 2022).

We use N_{OH} and N_{HI} for further absorption features from the THOR survey, and adopt a uniform excitation temperature for N_{OH} of $T_{ex} = 5$ K, for uniformity with the data presented here.

3.2. Molecular hydrogen column densities

For all but one line-of-sight OH absorption feature we detect ^{12}CO rotational lines (see Table A.1), and use these to infer the molecular gas content. We convert integrated ^{12}CO emission to molecular gas column density with a standard conversion factor of $\alpha_{CO} = 2 \times 10^{20}$ cm^{-2} (Bolatto et al. 2013). We rescale the ^{12}CO $J = 2-1$ observations by a typical line ratio of $R_{21/10} = 0.7$ (Sakamoto et al. 1997; Peñaloza et al. 2018; den Brok et al. 2021).

While a large fraction of the line-of sight OH absorption features show detections in the ^{13}CO (1–0) line, we decide to rely exclusively on a ^{12}CO conversion factor to derive molecular gas column densities. This choice was made as the rotational levels of weak ^{13}CO (1–0) detections are likely sub-thermally excited (e.g., Heyer et al. 2006). Previous studies have found that the molecular gas column densities derived from ^{13}CO emission at low densities may be underestimated when assuming local thermal equilibrium (LTE) conditions (Goldsmith et al. 2008; Heyer et al. 2009; Heiderman et al. 2010). We tested deriving N_{H_2} from the GRS ^{13}CO (1–0) line emission reported here under LTE conditions (assuming $T_{ex} = 10$ K), and found that N_{H_2} was systematically lower by a factor of 2 or more for most but the highest column densities when comparing it to N_{H_2} derived directly from ^{12}CO emission. We hence adopt N_{H_2} derived from ^{12}CO emission. The integrated emission from all spectral lines is reported in Table A.1 to enable more refined modeling in future studies (e.g., Roueff et al. 2021).

For comparison with the THOR survey, we retrieved ^{12}CO(1–0) spectra from the FUGIN survey to update the N_{H_2} estimates for the following line-of-sight absorption features from Rugel et al. (2018): THOR+28.806+0.174+79.5, THOR+31.242-0.110+79.5, THOR+31.242-0.110+83.5, THOR+39.565-0.040+24.0, and THOR+42.027-0.604+64.5. As described in Rugel et al. (2018), all data were convolved to 46″ before extracting the spectra at the source position.

The N_{H_2} estimates for OH absorption features associated with H II regions were adopted from Rugel et al. (2018), which used an excitation temperature of $T_{ex} = 20$ K for the GRS ^{13}CO (1–0) transition, applied an optical depth correction, and a standard conversion factor of $N(H_2) \sim 3.8 \times 10^5\, N(^{13}CO)$ (Pineda et al. 2008; Dickman 1978; Bolatto et al. 2013, and references therein). Given that the conversion does not account for the varying isotope ratio of ^{12}C/^{13}C with Galactocentric radius, we used the relation presented in Jacob et al. (2020) to rescale N_{H_2} for OH absorption features within the solar circle. The Galactocentric radius was derived using parameters of the Galactic rotation curve from Reid et al. (2019), as used in the bayesian distance calculator[3] (Reid et al. 2016). As the feature at 99.0 km s^{-1} for G29.935−0.053 presented in this work is associated with an H II region, we used the GRS ^{13}CO (1–0) emission, following the same procedure as described above. We exclude any OH absorption associated with the H II in G29.957−0.018, as the OH 1665 MHz transition is showing maser emission, which may affect the overall level population of the OH hyperfine splitting levels. After careful examination of the data, we used the ^{12}CO(1–0) emission as de-

---

[3] v2.4.1

scribed above also for THOR+32.272-0.226+22.5, as the column density from GRS ^{13}CO (1–0) was severely underestimated.

Bolatto et al. (2013) estimate the uncertainties for α_{CO} as 30%. Given that α_{CO} and $R_{21/10}$ may vary across the Milky Way, in particular in the diffuse ISM, the actual uncertainties in our sample are likely higher. We adopt an uncertainty for N_{H_2} of a factor of 2.

4. Results

4.1. OH line-of-sight absorption

All but one of the OH absorption features have been detected in ^{12}CO, 18/23 in ^{13}CO, and 5/23 in C^{18}O. Detection of ^{12}CO alone typically indicates gas at lower densities, while the detection of C^{18}O requires dense gas. 3/23 features are associated with molecular gas in the vicinity of H II regions (see Table A.1), the other 20/23 features represent line-of-sight absorption. To derive column densities we measured integral properties of all spectral lines over 23 different intervals in velocity. An example for OH in low-density environments is the component at $v = 37.0$ km s^{-1} towards the extra-galactic source G31.388−0.383. It is only weakly detected in ^{12}CO (2–1) emission. An example for OH absorption associated with dense gas as traced by C^{18}O is the deep OH absorption component at 56.5 km s^{-1} towards G21.347−0.629. The H I profile is also saturated here. We detect super-position of velocity components of low- and high-density gas: The OH 1667 MHz absorption feature along the line of sight towards the extra-galactic source G21.347−0.629 at 55 km s^{-1} (Fig. A.1) shows a combination of a narrow component (Δv ∼0.9 km s^{-1}) with a broader component (Δv ∼6 km s^{-1}), with their velocity centroids clearly shifted with respect to each other. The narrow and deeper component is detected in all CO isotopologues, and its detection in C^{18}O clearly indicates the presence of dense gas in this narrow component. The broad component is detected only in the ^{12}CO and ^{13}CO lines, which indicates gas of lower density. Towards $v = 7$ km s^{-1}, a narrow component with a linewidth of 0.7 km s^{-1} in OH 1667 MHz absorption and ^{13}CO emission is set on top of a broader component with a line width of 5.7 km s^{-1}, that is weak but detected in OH 1667 MHz absorption and readily visible in ^{12}CO emission.

Population inversion is a common feature in ground state HFS transitions of OH, particularly, in its satellite lines at 1612 and 1720 MHz. We detected 6/23 features simultaneously in both satellite lines, of which three show conjugate behavior of stimulated emission in the OH 1612 MHz line and absorption in the OH 1720 MHz line. One shows the reverse configuration of absorption in the OH 1612 MHz line and stimulated emission in the OH 1720 MHz line, and two show absorption in both main lines. The remaining features show typically weak absorption in either the 1612 MHz or the 1720 MHz line at the detection limit. Our sample does not contain clearly 'flipped' features which transition from emission to absorption, or vice versa, with increasing velocity, as has been described by Hafner et al. (2020). We note conjugated satellite line peaks towards G29.935−0.053 at $v = 101.2$ km s^{-1}, which are shifted from the peak velocity of the main lines at 99 km s^{-1}. However, we do not significantly detect a reversed feature at lower velocities. Figure A.1 indicates a potential reversal of the satellite lines across the broad velocity component at $v = 7$ km s^{-1} towards G21.347−0.629.

An example of OH main line inversion, which is typically seen in high-mass star forming regions (e.g., Beuther et al. 2019) pumped by strong infrared emission (e.g., Guibert et al. 1978) can be seen towards G29.957−0.018, in the compo-
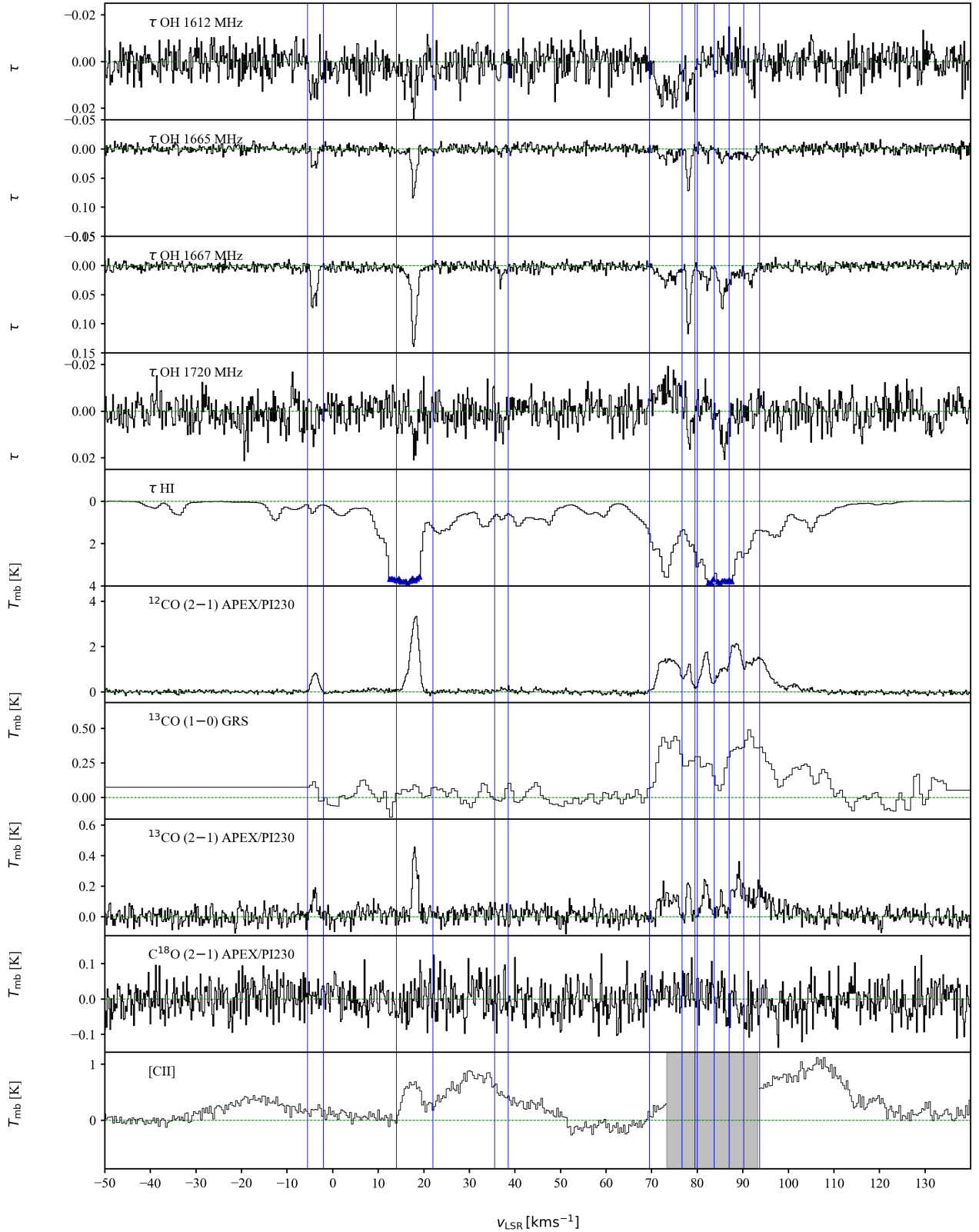
G31.388−0.383

Fig. 2. OH and H I absorption towards the extragalactic source G31.388−0.383. The first five panels show optical depths of the four OH lines and H I, as derived from the line-to-continuum ratio. For the H I absorption, blue triangles indicate saturated channels. Emission spectra of the three CO isotopologues are shown below that. The data is taken with APEX and from the GRS (Jackson et al. 2006) survey. The bottom most panel displays the SOFIA/upGREAT observations of the [C II] 158 μm line. Integration limits are shown as blue vertical lines. To emphasize that the OH and the H I lines are observed towards strong background sources, and are - with the exception of stimulated emission - seen in absorption, the axis of the optical depth is inverted, i.e., goes from positive to negative values.
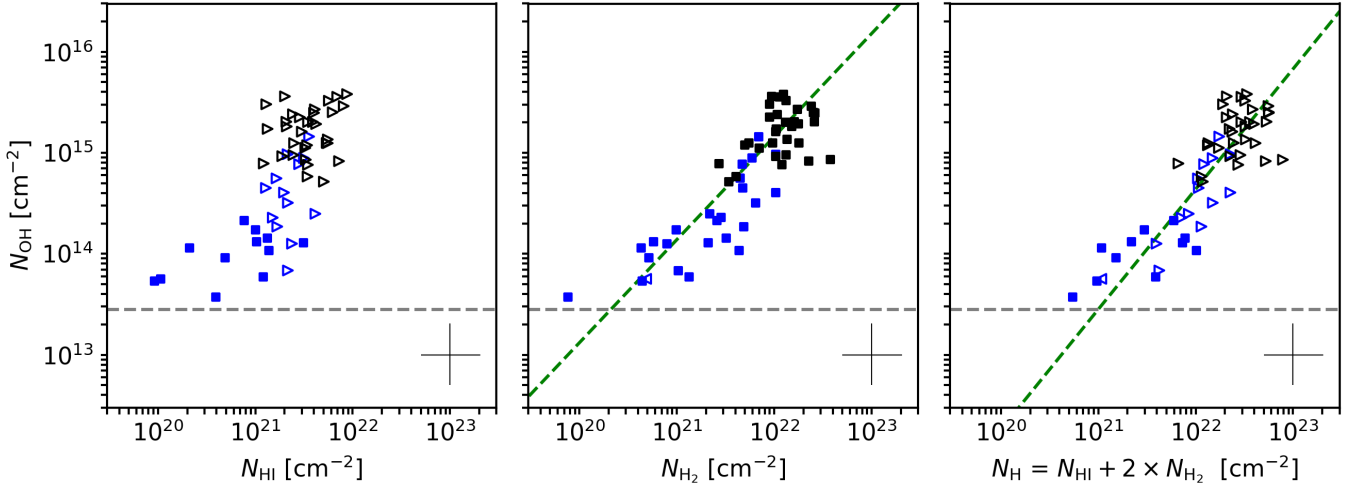
Fig. 3. OH column density vs. the column density of H I (*left*), H$_2$ (*middle*), and the column density of the total number of hydrogen nuclei (*right*). Features associated with line-of-sight absorption are shown in *blue*, features associated with H II regions in black ([Rugel et al. 2018](#)). The middle panel shows N_{OH} vs. N_{H_2}. Lower limits in case of saturated H I absorption in the *left* and *right* plots are indicated by triangles pointing to the right. There is one upper limit due to the non-detection of CO, which is indicated by triangles pointing to the left. Typical error bars are indicated in the lower right corner. The limit of a 3 σ detection is indicated by a dashed gray line. The green dashed line indicates the fit of a correlation to the data.
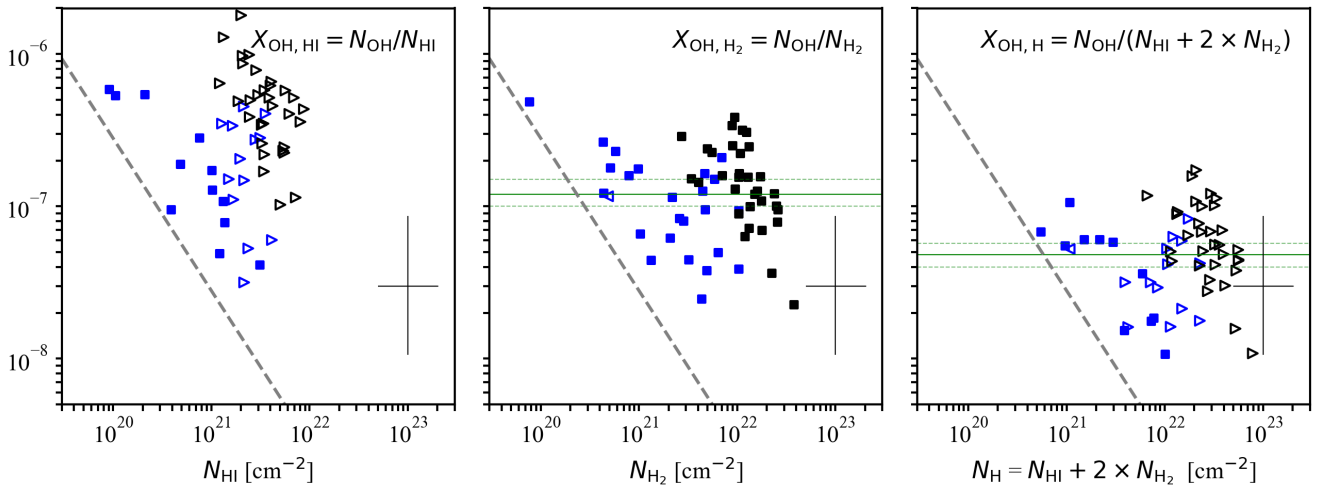
Fig. 4. Same as Fig. 3, but for the column density-averaged OH abundance. The dashed gray line indicates 3 σ sensitivity limits of the OH absorption observations presented here. The green lines indicate the median abundance (*solid*) and 1σ uncertainties (*dashed*).

nents around $100\,\mathrm{km\,s^{-1}}$ which is associated with an UCH II region. Maser emission in the OH 1665 MHz line is visible between 100–$105\,\mathrm{km\,s^{-1}}$. Both main lines show maser emission at $\sim107\,\mathrm{km\,s^{-1}}$ (Fig. A.2).

To summarize, we find that absorption in the OH 1665 MHz and OH 1667 MHz lines occurs in diffuse to dense environments. In the following sections, we discuss the OH abundance in these different ISM conditions.

4.2. The OH abundance in atomic and molecular gas

Given the occurrence of OH absorption in different ISM conditions noted in Sect. 4.1, this section analyzes the relation between OH absorption and tracers of different ISM gas phases. We trace the atomic gas component with the simultaneously recorded H I 21 cm line absorption. To trace phases dominated by molecular

hydrogen we make use of new and archival observations of CO. Both approaches have limitations - the H I 21 cm line saturates at high column densities, while CO may be less abundant or not present at all at low molecular hydrogen abundances. As CO emission is one of the most commonly used tracer of molecular gas in the literature, we adopt CO as our reference tracers of molecular hydrogen, and discuss limitations and implications below.

The probed ranges of N_{OH} and N_{H_2} extend to lower column densities than in the THOR sample. The OH observations in this study extend to column densities as low as $3.7\times10^{13}\,\mathrm{cm^{-2}}$ and up to $8.5\times10^{14}\,\mathrm{cm^{-2}}$. After rescaling N_{OH} to the same excitation temperature as the data presented here, the OH observations in THOR[4] ([Rugel et al. 2018](#)) probed higher column den-

---

[4] OH absorption detections presented here were not removed from the original sample presented in [Rugel et al. (2018)](#)

sities between 1.2×10^{14} and 3.8×10^{15} cm^{-2}. The column densities of molecular hydrogen as probed in this work by CO emission extend from $N_{H_2} = 7.7 \times 10^{19}$ cm^{-2} to 6.0×10^{22} cm^{-2}, whereas the OH detections reported in Rugel et al. (2018) occur at $N_{H_2} = 7.9 \times 10^{20}$ cm^{-2} to 4.7×10^{22} cm^{-2}.

In the following, we will jointly analyze both datasets. Due to higher sensitivities and higher spectral resolution (channel width of 0.2 km s^{-1} vs. 1.5 km s^{-1} for THOR) we are able to identify more narrow features in the new sample presented here.

Figure 3 compares the OH column densities to the column density of atomic hydrogen and CO-derived molecular hydrogen, as well as to the total column density of hydrogen nuclei, which is given as $N_H = 2 \times N_{H_2} + N_{HI}$. Comparing with the column density of atomic hydrogen, we see that the H I absorption is saturated for all OH features with $N_{HI} > 1.4 \times 10^{21}$ cm^{-2}. We identify 12 features in the dataset presented in this work for which the H I absorption is not saturated.

The middle panel compares N_{OH} with the column density of molecular hydrogen as traced by CO. The H_2 column densities are estimated from different isotopologues as well as different rotational transitions of CO (see Sect. 3.2). One feature in the new dataset does not have a counterpart in any CO line, namely the feature at 68.8 km s^{-1} toward G21.347−0.629. To investigate the relationship between OH and molecular hydrogen column densities, we fit the data with a power-law. To improve on previous estimates in Rugel et al. (2018) and to mitigate biases towards sub-linear trends, we fit a slope in logarithmic space with a least squares algorithm while properly accounting for uniform errors in both x and y directions, respectively (York 1966). We find the quantities to be related by a power law $N_{OH} \propto N_{H_2}^{m_{H_2}}$ with index $m_{H_2} = 1.0 \pm 0.1$. In the panel on the right-hand side of Fig. 3, we compare the OH column density to the total column density of hydrogen nuclei. Since the H I column density saturates in many instances, also N_H is a lower limit. If we took only the 12 data points for which N_{HI} is not saturated, the Spearman's rank coefficient is $r_s = 0.6$ with $p = 0.08$, which indicates that we cannot reject the null hypothesis at the present sample size. If we assume the contribution of N_{H_2} to N_H to dominate in most cases where N_{HI} saturates, we can also consider N_H estimates with saturated H I absorption. In this case we find an exponent for a power-law relation between N_{OH} and N_H of $m_H = 1.2 \pm 0.1$.

We investigate the OH abundance with respect to atomic, molecular and total hydrogen column density in Fig. 4. The median OH abundance with respect to molecular hydrogen of $X_{OH,H_2} = N_{OH}/N_{H_2} = 1.2^{+0.3}_{-0.2} \times 10^{-7}$. The upper and lower bounds indicate 16% and 84% confidence intervals of the abundance after bootstrapping the posterior distribution of the median over the error margins indicated in Sect. 3.2 (0.3 dex in N_{OH}, N_{H_2}, and N_{HI}). The median abundance with respect to the total column density of hydrogen nuclei is $X_{OH,H} = N_{OH}/N_H = 3.8^{+2.0}_{-1.4} \times 10^{-8}$, omitting features with saturated H I lines. The sample with non-saturated H I column densities spreads a large range in molecular gas fractions (see Fig. 5). This is holds true if we assume a lower spin temperature for N_{HI} (Fig. A.4). Sources with saturated H I column densities tend to occur in line-of-sight features with high molecular gas fraction, and the lower limits of N_{HI} would need to underestimate it by a factor of a few to significantly lower the molecular gas fractions. Including all estimates of N_H, the median abundance is $X_{OH,H} = 4.8^{+0.9}_{-0.8} \times 10^{-8}$, which is only slightly higher than the result with H I detections only.

The abundances for line-of-sight components are $X_{OH,H_2} = 1.1^{+0.7}_{-0.5} \times 10^{-7}$ and $X_{OH,H} = N_{OH}/N_H = 3.8^{+2.1}_{-1.4} \times 10^{-8}$. This is slightly lower than the abundances for OH associated with H II
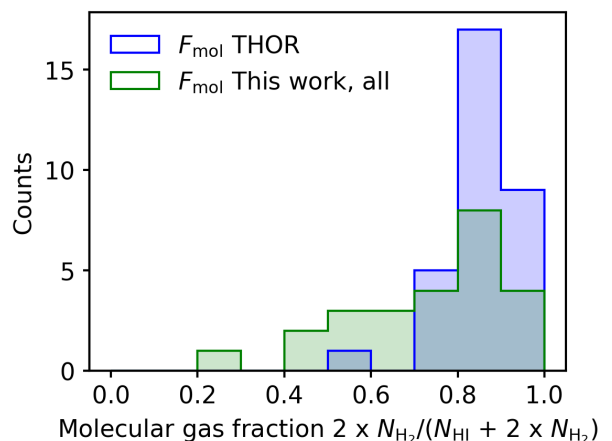
Fig. 5. Distribution of molecular gas fraction in this work (*green*) in comparison to the sample from THOR (*blue*). Many of the features included in both samples are upper limits on the molecular gas fraction, as the H I absorption saturate. We hence highlight the sub-sample of features with non-saturating H I absorption presented in this work (*red*).

regions are $X_{OH,H_2} = 1.4^{+3.7}_{-2.9} \times 10^{-7}$ and $X_{OH,H} = 5.9^{+1.4}_{-1.2} \times 10^{-8}$. Figure 6 shows the molecular and total hydrogen abundance vs. Galactocentric radius. While slight variations may be present, the Spearman's rank test yielded $p > 0.1$ for any correlation between X_{OH,H_2} or $X_{OH,H}$ and R_{GC}, both for line-of-sight components and molecular clouds associated with H II regions individually, as well as all data combined.

4.3. Detections of the [C II] 158 µm emission towards OH absorption components

The [C II] observations for G31.388−0.383 and G29.935−0.053 are shown Figs. 2 and A.3, respectively. We find widespread [C II] emission in both spectra originating from different velocity components along the line of sight. Given its strength and velocity, the main component of the [C II] emission in G29.935−0.053 is dominated by PDR emission from the H II region complex. G31.388−0.383 shows enhanced [C II] emission around 100 km s^{-1} and is affected by contamination in the reference position between 73 and 93 km s^{-1} (Fig. B.2). Below, we discuss [C II] emission as it occurs in conjunction with OH main line absorption.

For G29.935−0.053, Fig. A.3 does not show [C II] 158 µm emission that can be uniquely associated with line-of-sight OH absorption. While the [C II] 158 µm emission at $v = 51$ km s^{-1} is close in velocity to an OH absorption feature, its peak does not match, but rather seems to be associated with the deep H I absorption feature, as it spans a similar range in velocity. The lower emission between 0 and 30 km s^{-1} appears to be consistent between different observing dates and reference positions, and is seen in all of the pixels (Fig. B.5). It could indicate absorption, although we note baseline ripples of similar strength. As a confident estimate of the continuum level was not possible, we do not discuss the feature here further.

For G31.388−0.383 (Fig. 2), we see broad [C II] 158 µm emission towards $v = 37$ km s^{-1}. However, we cannot identify a specific [C II] 158 µm emission feature associated in velocity with the OH absorption. Towards $v = 18$ km s^{-1} we detect significant [C II] 158 µm emission which is potentially associated with OH
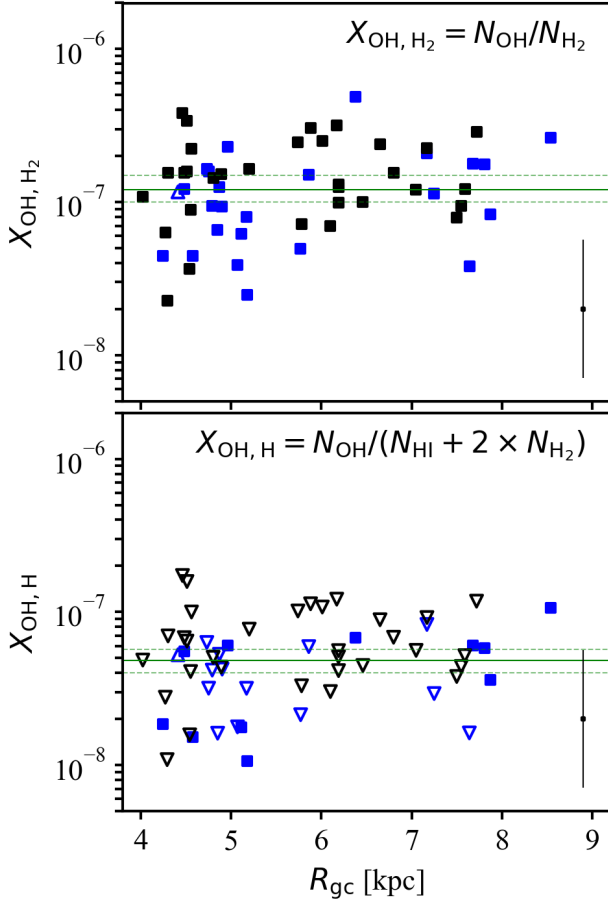
Fig. 6. Same as Fig. 4 but for X_{OH,H_2} and $X_{OH,H}$ vs. R_{GC}.

absorption. We discuss its gas content in the below. After removing contributions from the underlying broader emission profile, the component at $18\,\mathrm{km\,s^{-1}}$ yields an integrated [C II] $158\,\mu m$ emission of $1.8\,\mathrm{K\,km\,s^{-1}}$.

We estimate the column density of the [C II] $158\,\mu m$ emission, re-arranging equation 26 for the optically thin case from Goldsmith et al. (2012) (see also Beuther et al. 2022):

$$N_{CII} = 2.9 \times 10^{15} \times \left[1 + 0.5 e^{(91.25/T_{kin})} \times \left(1 + \frac{2.4 \times 10^{-6}}{n R_{ul}} \right) \right]$$
$$\times \int T_{mb} dv$$

(3)

We assume a kinetic temperature of $T_{kin} = 100\,\mathrm{K}$, a collision rate coefficient[5] of $R_{ul} = 5 \times 10^{-10}$ for collisions with ortho- and para-H_2 (4.7×10^{-10} and, respectively, 5.5×10^{-10}; Schöier et al. 2005; Lique et al. 2013) in an equal ratio, and densities of $n = 10^3\,\mathrm{cm^{-3}}$. We find the column density to be $N_{C^+} = 4.3 \times 10^{16}\,\mathrm{cm^{-2}}$.

In Sect. 3.2, we derived the H_2 column density from the integrated ^{12}CO emission directly. Here, we estimate the ^{12}CO column density from its $J = 2\text{--}1$ emission with an excitation temperature of $T_{ex} = 10\,\mathrm{K}$ using equation 79 in Mangum & Shirley (2015), and obtain $N_{^{12}CO} = 7.1 \times 10^{15}\,\mathrm{cm^{-2}}$. While we do not have tracers of neutral carbon available, this indicates considerable ionization fractions, consistent with models of translucent

---

[5] https://home.strw.leidenuniv.nl/~moldata/C+.html

---

clouds (van Dishoeck & Black 1988). We note that 1667 MHz OH absorption appears to consist of multiple components. A narrow one, which is detected in both ^{12}CO and ^{13}CO emission, as well as a broader one, which is only detected in ^{12}CO. The ^{13}CO emission has a line width of $1.2\,\mathrm{km\,s^{-1}}$, which is considerably more narrow than the [C II] $158\,\mu m$ emission with a FWHM of $3.7\,\mathrm{km\,s^{-1}}$. It may be that OH is picked up from both a diffuse, broad component with high carbon ionization fraction, as well as denser, predominantly molecular component.

4.4. C$^+$ in the H II region complex G29.935−0.053

The [C II] $158\,\mu m$ emission associated with G29.935−0.053 shows complex line shapes, potentially affected by self-absorption (Fig. A.3). Figure 7 shows the radio continuum emission at 1.4 GHz in contours across G29.935−0.053, together with the positions observed during the SOFIA observations. Pixel 0 (see Sect. 3.1) and pixel 5 are associated with peaks of the continuum emission, while the other pixels sample different parts of the HII region complex. The complete data are presented in Fig. A.5.

The [C II] $158\,\mu m$ emission at pixel 0 extends between $76\,\mathrm{km\,s^{-1}}$ and $127\,\mathrm{km\,s^{-1}}$ and contains three distinguishable emission peaks. The [O I] $63\,\mu m$ emission shows a similar line shape (Fig. B.1). Recent studies have interpreted [C II] $158\,\mu m$ and [O I] $63\,\mu m$ emission from H II region complexes as a complex interplay of warm background emission and cold foreground absorption (Guevara et al. 2020, 2024), motivated by simultaneous detections of [^{13}C II] and the [O I] $145\,\mu m$ emission, which are typically optically thin and dominated by the warm background emission. No measurements of the [O I] $145\,\mu m$ emission are available for this study. A search for [^{13}C II] emission shows faint features at the correct velocities, but remains in the end inconclusive: The upGREAT SOFIA observations in the rest frame of the [^{13}C II] $F=1\text{--}0$ and [^{13}C II] $F=1\text{--}1$ lines (Fig. B.6) indicates an emission peak at rest velocities of G29.935−0.053 in the [^{13}C II] $F=1\text{--}0$ line, but it is over-posed by potential absorption, baseline ripples, and Galactic emission. The [^{13}C II] $F=1\text{--}1$ line, located at lower frequencies than the [C II] $158\,\mu m$ line, is the weakest of the three hyperfine splitting transitions and only shows marginal emission. Without a clear identification of the [^{13}C II] hyperfine-splitting transitions and no availability of the [O I] $145\,\mu m$, the background and foreground components contributing to the [C II] $158\,\mu m$ and the [O I] $63\,\mu m$ cannot be disentangled.

We point out that the ^{12}CO emission bears resemblance to the three-peak structure of the [C II] $158\,\mu m$ emission. To some extent this also holds for the ^{13}CO emission. Both show a trough at similar velocities as the [C II] $158\,\mu m$ profile. The strongest peak of the $C^{18}O$ emission is aligned with the trough in the ^{12}CO and ^{13}CO emission, indicating the presence of dense gas in this component, and suggesting that ^{12}CO and ^{13}CO lines are both optically thick at these velocities. This dense gas component also matches the velocity of the main line OH absorption peak. The $C^{18}O$ line shows several other peaks, both at lower velocities towards $93\,\mathrm{km\,s^{-1}}$, and at higher velocities at $102\,\mathrm{km\,s^{-1}}$ and $110\,\mathrm{km\,s^{-1}}$. The feature at $102\,\mathrm{km\,s^{-1}}$ falls into the red tail of the OH main line absorption feature. Given the alignment of the OH absorption, the $C^{18}O$ emission, and the trough in [C II] $158\,\mu m$ emission over many of the pixels of the SOFIA observation (Fig. A.5), the trough in the [C II] $158\,\mu m$ and the [O I] $63\,\mu m$ emission may corresponds to absorption of a colder foreground component. Additional observational constraints, however, are necessary to resolve the geometry of the region giving rise to the observed line profiles.
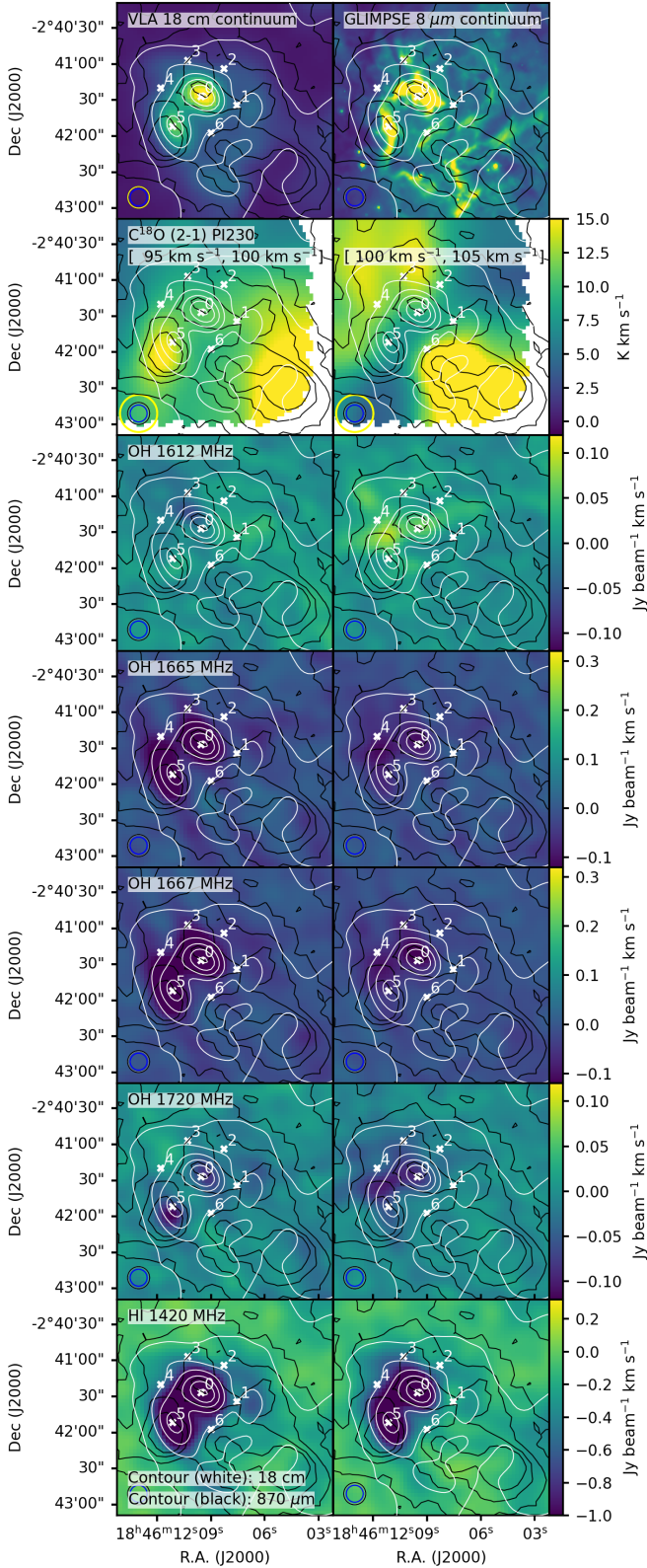
Fig. 7. Distribution of VLA 18 cm and GLIMPSE 8 μm continuum emission (top row Benjamin et al. 2003) in G29.935−0.053, with contours of ATLASGAL 870 μm emission (black; at 0.5, 1.0, 1.5 and 2 Jy beam^{-1} Schuller et al. 2009) and VLA 18 cm continuum (white; in steps of 0.1 Jy beam^{-1}, starting at 0.03 Jy beam^{-1}). The beam of both observations is indicated with a black circle in the lower left. The positions of the upGREAT LFA pixels are indicated, and the beamsize indicated in blue. The following rows show spectral lines integrated over 95–100 km s^{-1} and 100–105 km s^{-1} in the left and right panels, respectively.

4.5. Spatial and spectral variation of the OH excitation

Resolved 18 cm continuum observations in G29.935−0.053 enable us to investigate spatial and spectral variation of the excitation conditions of OH. Figure 7 indicates clumps of dense gas as traced by 870 μm emission from cold dust spatially surrounding 18 cm continuum emission. The Galactic Legacy Infrared Midplane Survey Extraordinaire (GLIMPSE) 8 μm map traces emission from poly aromatic hydrocarbons (PAHs) which appears to lie at interfaces between cm-continuum emission and dust emission, indicating the location of PDR regions. The continuum emission towards pixels 0, 2, 3, 4 appears to lie behind a layer of molecular and atomic gas, as OH and H I is detected in absorption (Figure A.5). Radio recombination lines at 5 cm appear to peak redshifted (towards Pixels 2, 3, 4 and 5) or at similar velocities (Pixel 0) as the OH absorption, indicating expansion away in the back of the molecular gas emission. Pixel 1 and 6 do not show OH absorption, indicating that the continuum emission may lie in front of the bulk of the molecular gas. The dense molecular gas appears to be distributed in different spatial and spectral components across the region. The integrated C^{18}O (2 − 1) emission between 95 − 100 km s^{-1} appears to peak towards the 870 μm emission peak, indicating that this velocity component may trace cold, dense molecular clumps. Emission at velocities between 100 − 105 km s^{-1} appears to extend towards the southwest and northeast of the H II region.

The OH satellite lines peak at redder velocities than the minimum of the OH main line absorption and maximum of the C^{18}O emission. This indicates the presence of distinct velocity components contributing to the OH lines, as also the CO emission in Fig. 7 appears to originate from different spatial locations inside G29.935−0.053 for different velocity ranges. Also for the OH main lines, blueshifted components appear to be strongest towards the peak of the continuum emission and close to the peak of the 870 μm emission. The redshifted component appears to originate offset towards the northeast. The satellite line absorption (1720 MHz) and emission (1612 MHz) appear to follow the distribution of the redshifted component of the OH main line absorption.

5. Discussion

Section 4.1 shows that gas at different densities appears to contribute to OH absorption, as inferred from the detection statistics of CO isotopologs. This is in agreement with findings in the literature: For example, OH has been found in PDRs at densities of $n_{H_2} \sim 10^6$ cm^{-3} (e.g., DR21; Jones et al. 1994; Koley 2023), and at intermediate to low densities in molecular cloud envelops of $n < 10^3$ cm^{-3} (TMC-1; Ebisawa et al. 2019). Busch et al. (2019) found an upper limit for the volume density of OH in CO-dark gas of $n < 10^2$ cm^{-3} through chemical modeling, and Busch et al. (2021) inferred extremely low average densities of as low as $n \sim 7 \times 10^{-3}$ cm^{-3} for a layer of CO-dark OH gas in the Outer Galaxy. The consistent appearance of OH throughout very different environments is likely related to its natural appearance in oxygen chemistry (e.g., van Dishoeck et al. 2013, and references therein), and the HFS transitions of the rotational ground state of OH are easily excited due to their small energy difference.

The initial motivation for this study was to follow-up and search for OH features which are candidates for tracing CO-dark gas as a potential tracer for the transition regions between atomic and molecular gas. Our investigations only revealed one feature without a simultaneous detection of carbon monoxide, at least within the sensitivities and angular resolution of the data

at hand. This detection rate appears to be in agreement with previous studies: Li et al. (2018) found two sources significantly above our 3σ limit of 3-4$\times$10^{13} cm^{-2} without a counterpart CO detection (there are 3 more at our 3σ limit). Conversely, they also find several OH features at similar column densities which show CO counterparts. Both the sample presented here and the THOR sample indicate OH absorption features at intermediate molecular gas fractions (<0.8; Fig. 5), i.e., for which the hydrogen gas content is not fully dominated by molecular hydrogen. These may fall into the diffuse molecular interstellar cloud type (Snow & McCall 2006). A particularly interesting feature in this context is the OH absorption feature at 37 km s^{-1} towards G31.388−0.383, which shows a highly elevated $X_{\mathrm{OH,H_2}}$ but an average $X_{\mathrm{OH,H}}$ value at $R_{\mathrm{GC}} = 6.4$ kpc in Fig. 6, indicating a large atomic gas fraction. We also note that α_{CO} may be significantly underestimated at $N_{\mathrm{H_2}} = 0.8 \times 10^{20}$ cm^{-2} due to low CO abundances (van Dishoeck & Black 1988; Liszt 2007).

Our findings of a linear relation between N_{OH}, $N_{\mathrm{H_2}}$ and N_{H} is in agreement with previous studies. Xu et al. (2016) find a linear relation between emission in the OH 1665 MHz line and dust extinction in the Taurus molecular cloud. Liszt & Lucas (1996) find OH absorption to be tightly correlated with HCO$^+$. Our results show OH abundances which agree well with other measurements within the uncertainties and the scatter of our sample (e.g., Goss 1968; Crutcher 1979; Jacob et al. 2022; Albertsson et al. 2014). While the median abundance is slightly lower in more diffuse line-of-sight clouds than in dense molecular clouds associated within H II regions, they agree well within errors. We do not detect significant abundance variations with Galactocentric radius within the Solar circle. The measured abundances agree well with chemical models, which predict abundances between $10^{-8} - 10^{-7}$ for $A_V < 1$, which can increase to $\sim 10^{-6}$ for $A_V > 1$ (e.g., Hollenbach et al. 2009, 2012).

Towards high densities in star forming regions and in the presence of strong infrared radiation fields, the excitation structure of the OH hyperfine splitting transitions (e.g., Nguyen-Q-Rieu et al. 1976) may vary from diffuse clouds, as indicated by the maser emission in G29.957−0.018 around 100 km s^{-1}. A combined modeling of the hyperfine splitting transitions of OH at 18 cm with absorption of the OH rotational transitions into the ground state at far-infrared wavelengths (e.g., Wiesemeyer et al. 2012; Jacob et al. 2022) can further constrain the excitation structure. For OH absorption and emission features associated with high-mass star formation, previous studies revealed significant pumping by the far infrared radiation field (e.g., Goicoechea & Cernicharo 2002; Csengeri et al. 2012).

The analysis of the OH abundance presented here relies on CO as tracer of the bulk molecular gas, as measurements of CO are readily available and provide the necessary spectral information. However, we acknowledge that this introduces biases in the presented analysis: At the low end, it likely underestimates the true H$_2$ column density given the presence of significant fractions of CO-dark gas in diffuse ISM regions (e.g., Grenier et al. 2005; Pineda et al. 2013). This would imply slightly steeper relations than determined in Sect. 4.2. The abundance itself, however, does not show significant trends towards higher abundances at low H$_2$ column densities (Fig. 4) after accounting for the scatter and the approximate sensitivity limit (gray dashed line in Fig. 4). Indeed, if CO was underrepresenting the H$_2$ column density, an expectation could be that the OH abundance increases with increasing Galactocentric radius as we derive $N_{\mathrm{H_2}}$ from the CO emission. While Pineda et al. (2013) indicate an increase in the CO-dark gas fraction by a factor of ~3 between $R_{\mathrm{GC}} = 4$ kpc and $R_{\mathrm{GC}} = 8$ kpc, our data do not show evidence for a significant trend

of the OH abundance with Galactocentric radius, neither for OH in line-of-sight absorption features, nor for OH associated with star formation (Fig. 6). This indicates that potential contributions of CO-dark gas to $N_{\mathrm{H_2}}$ may be of limited impact, at least for the data presented here. Nevertheless, a comparison also to more suitable molecular gas tracers in the diffuse ISM, i.e., 3D dust maps (e.g., Mullens et al. 2024), HCO$^+$ (e.g., Rybarczyk et al. 2022; Kim et al. 2023) or hydride absorption (e.g., Jacob et al. 2022), may be beneficial to further assess the OH abundances in the regime where CO ceases to be a reliable molecular gas tracer.

While the [C II] 158 μm line has been used as a tracer of CO-dark gas (e.g., Pineda et al. 2013), not all of the emission is molecular-gas dominated (e.g., Franeck et al. 2018; Ebagezio et al. 2024). As we find OH in lines of sight which have low molecular gas fractions (Sect. 3.1), we note at the same time for G29.935−0.053 and G31.388−0.383 that not all of the [C II] 158 μm emission has clear molecular gas counterparts. Some of the extended [C II] 158 μm emission at velocities close to the main molecular gas velocities may be tracing molecular cloud assembly, as suggested in observations (Schneider et al. 2023), and simulations (Clark et al. 2019). Finding the line width of the [C II] 158 μm emission component to be $\Delta v = 3.4$ km s^{-1} in G31.388−0.383 – broader than the main molecular component – may itself be a signature of molecular clouds in formation (Heyer et al. 2022). The feature is slightly stronger ($T_{\mathrm{mb,peak}} = 0.55$ K) than previous detections of [C II] 158 μm emission in the diffuse ISM (Goldsmith et al. 2018). Some of the population of features with weak [C II] 158 μm emission may have hence been missed at our sensitivity of $\sigma \sim 0.1$ K, as well as due to line-of-sight confusion in velocity.

The OH observations towards G29.935−0.053 appear to resemble parts of the common phenomenon "satellite line reversal" seen in several H II regions (Hafner et al. 2020), which is an opposing pattern of the OH satellite lines where the OH 1612 MHz line changes from absorption to inversion with increasing velocity, while the OH 1720 MHz changes from inversion to absorption. Even though not all parts of the profile are significantly detected, the identified parts of the features are in agreement with this phenomenon. Also, incomplete detections of the full profile in the OH satellite lines appear to be common (Rugel et al. 2018). The resemblance with the global pattern makes the observed line profiles in G29.935−0.053 unlikely to be related to any geometrical alignments unique to this object. Hafner et al. (2020) attribute the OH 1612 MHz inversion layer to a quiescent gas component into which the H II region is expanding, while the blueshifted OH 1720 MHz inversion originates from shocked gas itself. A detailed account of such an expansion scenario has been given in M17, as presented in Pellegrini et al. (2007, see also Brogan & Troland 2001; Brogan et al. 1999), who find blueshifted OH and H I absorption tracing an expanding shell into the ambient ISM. The ambient gas is associated with a redshifted component. Spatially, M17 also shows arcs in H I and OH absorption associated with the expansion. Applied to G29.935−0.053, the extended redshifted component would represent the molecular medium the H II region is expanding into, while the blueshifted absorption would be associated with the expanding shell itself. Albeit no proper 3D model of the H II complex is available for a full confirmation, the scenario proposed by Hafner et al. (2020) seems to be largely in agreement with the observations found here. A potential caveat would be that the blueshifted OH absorption component appears to coincide with the velocity of the dense gas clump towards pixel 5, for which the blueshifted component could be associated with the dense molecular gas itself which the HII region is expanding into at one side, instead being

solely related to the expansion of the shell. A larger sample of resolved studies of OH absorption can shed further light on this problem.

6. Conclusion

We present high-sensitivity OH and H I absorption observations at cm-wavelengths with the VLA towards four lines of sight. These are follow-up observations of the THOR survey, initially to investigate faint OH absorption from diffuse interstellar clouds and cloud envelopes, but which were found to also trace OH in high-mass star forming regions. For two lines of sight, we compared the OH lines with [C II] 158 μm emission observations from upGREAT at SOFIA, as well as deep CO $(2-1)$ lines with the PI230 receiver at the APEX telescope.

- We find OH absorption at 1665 MHz and 1667 MHz in a variety of ISM environments, both associated with dense and diffuse gas, and with gas with intermediate- and high-molecular gas fractions. We detect one feature which is without a CO counterpart. We compare OH with hydrogen column densities as derived from CO and HI. Within uncertainties we find $N_{\rm OH}$ linearly correlated both with respect to $N_{\rm H}$, where this is the total hydrogen column density, with a fitted power-law exponent of $m_{\rm H} = 1.2 \pm 0.1$, and with respect to $N_{\rm H_2}$ ($m_{\rm H_2} = 1.0 \pm 0.1$). The derived OH abundances, $X_{\rm OH,H_2} = N_{\rm OH}/N_{\rm H_2} = 1.2^{+0.3}_{-0.2} \times 10^{-7}$ and $X_{\rm OH,H} = N_{\rm OH}/(2 \times N_{\rm H_2} + N_{\rm HI}) = 4.8^{+0.9}_{-0.8} \times 10^{-8}$, agree well with previous studies within the uncertainties and scatter of our measurements.
- We detect [C II] 158 μm emission at similar velocities as an OH absorption feature towards G31.388−0.383. The estimated column density of ionized carbon exceeds the column density of carbon monoxide, indicating that significant fractions of the carbon in this feature are ionized, although the fraction of C$^+$ gas associated with the OH absorption is not clear. Other associations with line-of-sight OH absorption are not detected or remain ambiguous. G29.935−0.053 shows [C II] 158 μm emission from PDRs in the H II region complex with indications of [C II] 158 μm self-absorption, which is potentially associated with OH absorption.
- G29.935−0.053 shows spectrally varying excitation conditions in all four OH lines, which manifest themselves in different spatial morphologies of the optical depths of the OH satellite lines (OH 1612/1720 MHz) as compared to the main lines (OH 1665/1667 MHz). This confirms previous studies in that both OH absorption and stimulated emission can originate from multiple gas components in an H II region complex.

For the mid-plane of the Milky Way disk, we find that the detection of true CO-dark gas remains challenging. The relevance of the hyperfine splitting transitions of hydroxyl at 18 cm as tracer of the onset of molecular cloud formation is yet to be further explored. Ray-tracing of simulations, observations of the OH 18 cm lines with future radio telescopes, or complementary investigations of transitions of OH at other frequencies (e.g., Jacob et al. 2022, Busch et al., in prep.) will help to address this question.

References

Albertsson, T., Indriolo, N., Kreckel, H., et al. 2014, ApJ, 787, 44
Allen, R. J., Hogg, D. E., & Engelke, P. D. 2015, AJ, 149, 123
Beckwith, S., Evans, II, N. J., Gatley, I., Gull, G., & Russell, R. W. 1983, ApJ, 264, 152

Beltrán, M. T., Olmi, L., Cesaroni, R., et al. 2013, A&A, 552, A123
Benjamin, R. A., Churchwell, E., Babler, B. L., et al. 2003, PASP, 115, 953
Beuther, H., Bihr, S., Rugel, M., et al. 2016, A&A, 595, A32
Beuther, H., Schneider, N., Simon, R., et al. 2022, A&A, 659, A77
Beuther, H., van Dishoeck, E. F., Tychoniec, L., et al. 2023, A&A, 673, A121
Beuther, H., Walsh, A., Wang, Y., et al. 2019, A&A, 628, A90
Bolatto, A. D., Wolfire, M., & Leroy, A. K. 2013, ARA&A, 51, 207
Brogan, C. L. & Troland, T. H. 2001, ApJ, 560, 821
Brogan, C. L., Troland, T. H., Roberts, D. A., & Crutcher, R. M. 1999, ApJ, 515, 304
Brunthaler, A., Menten, K. M., Dzib, S. A., et al. 2021, A&A, 651, A85
Burkhart, B., Dharmawardena, T. E., Bialy, S., et al. 2025, Nature Astronomy [arXiv:2504.17843]
Busch, M. P., Allen, R. J., Engelke, P. D., et al. 2019, ApJ, 883, 158
Busch, M. P., Engelke, P. D., Allen, R. J., & Hogg, D. E. 2021, ApJ, 914, 72
Chevance, M., Krumholz, M. R., McLeod, A. F., et al. 2023, in Astronomical Society of the Pacific Conference Series, Vol. 534, Protostars and Planets VII, ed. S. Inutsuka, Y. Aikawa, T. Muto, K. Tomida, & M. Tamura, 1
Clark, P. C., Glover, S. C. O., Ragan, S. E., & Duarte-Cabral, A. 2019, MNRAS, 486, 4622
Crutcher, R. M. 1979, ApJ, 234, 881
Csengeri, T., Menten, K. M., Wyrowski, F., et al. 2012, A&A, 542, L8
Dawson, J. R., Jones, P. A., Purcell, C., et al. 2022, MNRAS, 512, 3345
den Brok, J. S., Chatzigiannakis, D., Bigiel, F., et al. 2021, MNRAS, 504, 3221
Dickey, J. M., Crovisier, J., & Kazes, I. 1981, A&A, 98, 271
Dickey, J. M., Dempsey, J. M., Pingel, N. M., et al. 2022, ApJ, 926, 186
Dickman, R. L. 1978, ApJS, 37, 407
Dobbs, C. L., Krumholz, M. R., Ballesteros-Paredes, J., et al. 2014, in Protostars and Planets VI, ed. H. Beuther, R. S. Klessen, C. P. Dullemond, & T. Henning, 3–26
Ebagezio, S., Seifried, D., Walch, S., & Bisbas, T. G. 2024, A&A, 692, A58
Ebisawa, Y., Sakai, N., Menten, K. M., & Yamamoto, S. 2019, ApJ, 871, 89
Franeck, A., Walch, S., Seifried, D., et al. 2018, MNRAS, 481, 4277
Gerin, M., Ruaud, M., Goicoechea, J. R., et al. 2015, A&A, 573, A30
Glover, S. C. O. & Clark, P. C. 2012, MNRAS, 421, 9
Goicoechea, J. R. & Cernicharo, J. 2002, ApJ, 576, L77
Goicoechea, J. R., Joblin, C., Contursi, A., et al. 2011, A&A, 530, L16
Goldsmith, P. F., Heyer, M., Narayanan, G., et al. 2008, ApJ, 680, 428
Goldsmith, P. F., Langer, W. D., Pineda, J. L., & Velusamy, T. 2012, ApJS, 203, 13
Goldsmith, P. F., Pineda, J. L., Neufeld, D. A., et al. 2018, ApJ, 856, 96
Goss, W. M. 1968, ApJS, 15, 131
Grenier, I. A., Casandjian, J.-M., & Terrier, R. 2005, Science, 307, 1292
Guevara, C., Stutzki, J., Ossenkopf-Okada, V., et al. 2024, A&A, 690, A294
Guevara, C., Stutzki, J., Ossenkopf-Okada, V., et al. 2020, A&A, 636, A16
Guibert, J., Rieu, N. Q., & Elitzur, M. 1978, A&A, 66, 395
Güsten, R., Nyman, L. Å., Schilke, P., et al. 2006, A&A, 454, L13
Hafner, A., Dawson, J. R., Nguyen, H., et al. 2023, PASA, 40, e015
Hafner, A., Dawson, J. R., & Wardle, M. 2020, MNRAS, 497, 4066
Heiderman, A., Evans, II, N. J., Allen, L. E., Huard, T., & Heyer, M. 2010, ApJ, 723, 1019
Heiles, C. & Troland, T. H. 2003, ApJ, 586, 1067
Heyer, M., Goldsmith, P. F., Simon, R., Aladro, R., & Ricken, O. 2022, ApJ, 941, 62
Heyer, M., Krawczyk, C., Duval, J., & Jackson, J. M. 2009, ApJ, 699, 1092
Heyer, M. H., Williams, J. P., & Brunt, C. M. 2006, ApJ, 643, 956
Hollenbach, D., Kaufman, M. J., Bergin, E. A., & Melnick, G. J. 2009, ApJ, 690, 1497
Hollenbach, D., Kaufman, M. J., Neufeld, D., Wolfire, M., & Goicoechea, J. R. 2012, ApJ, 754, 105
Jackson, J. M., Rathborne, J. M., Shah, R. Y., et al. 2006, ApJS, 163, 145
Jacob, A. M., Menten, K. M., Wiesemeyer, H., et al. 2020, A&A, 640, A125
Jacob, A. M., Neufeld, D. A., Schilke, P., et al. 2022, ApJ, 930, 141
Jones, K. N., Field, D., Gray, M. D., & Walker, R. N. F. 1994, A&A, 288, 581
Khan, S., Rugel, M. R., Brunthaler, A., et al. 2024, A&A, 689, A81
Kim, W. J., Schilke, P., Neufeld, D. A., et al. 2023, A&A, 670, A111
Koley, A. 2023, PASA, 40, e046
Langer, W. D., Velusamy, T., Pineda, J. L., Willacy, K., & Goldsmith, P. F. 2014, A&A, 561, A122
Li, D., Tang, N., Nguyen, H., et al. 2018, ApJS, 235, 1
Lique, F., Werfelli, G., Halvick, P., et al. 2013, J. Chem. Phys., 138, 204314
Liszt, H. & Lucas, R. 1996, A&A, 314, 917
Liszt, H. & Lucas, R. 2002, A&A, 391, 693
Liszt, H. S. 2007, A&A, 476, 291
Mangum, J. G. & Shirley, Y. L. 2015, PASP, 127, 266
Motte, F., Nguyen Luong, Q., Schneider, N., et al. 2014, A&A, 571, A32
Mullens, E., Zucker, C., Murray, C. E., & Smith, R. 2024, ApJ, 966, 127
Murray, C. E., Stanimirović, S., Goss, W. M., et al. 2018, ApJS, 238, 14
Nguyen, H., Dawson, J. R., Miville-Deschênes, M. A., et al. 2018, ApJ, 862, 49
Nguyen-Q-Rieu, Winnberg, A., Guibert, J., et al. 1976, A&A, 46, 413

Paradis, D., Dobashi, K., Shimoikura, T., et al. 2012, A&A, 543, A103
Peñaloza, C. H., Clark, P. C., Glover, S. C. O., & Klessen, R. S. 2018, MNRAS, 475, 1508
Pellegrini, E. W., Baldwin, J. A., Brogan, C. L., et al. 2007, ApJ, 658, 1119
Pineda, J. E., Arzoumanian, D., Andre, P., et al. 2023, in Astronomical Society of the Pacific Conference Series, Vol. 534, Protostars and Planets VII, ed. S. Inutsuka, Y. Aikawa, T. Muto, K. Tomida, & M. Tamura, 233
Pineda, J. E., Caselli, P., & Goodman, A. A. 2008, ApJ, 679, 481
Pineda, J. L., Langer, W. D., Velusamy, T., & Goldsmith, P. F. 2013, A&A, 554, A103
Planck Collaboration, Abergel, A., Ade, P. A. R., et al. 2014, A&A, 571, A11
Planck Collaboration, Ade, P. A. R., Aghanim, N., et al. 2011, A&A, 536, A19
Reid, M. J., Dame, T. M., Menten, K. M., & Brunthaler, A. 2016, ApJ, 823, 77
Reid, M. J., Menten, K. M., Brunthaler, A., et al. 2019, ApJ, 885, 131
Remy, Q., Grenier, I. A., Marshall, D. J., & Casandjian, J. M. 2018, A&A, 611, A51
Risacher, C., Güsten, R., Stutzki, J., et al. 2016, A&A, 595, A34
Roueff, A., Gerin, M., Gratier, P., et al. 2021, A&A, 645, A26
Rugel, M. R., Beuther, H., Bihr, S., et al. 2018, A&A, 618, A159
Rybarczyk, D. R., Stanimirović, S., Gong, M., et al. 2022, ApJ, 928, 79
Sakamoto, S., Hasegawa, T., Handa, T., Hayashi, M., & Oka, T. 1997, ApJ, 486, 276
Schneider, N., Bonne, L., Bontemps, S., et al. 2023, Nature Astronomy, 7, 546
Schöier, F. L., van der Tak, F. F. S., van Dishoeck, E. F., & Black, J. H. 2005, A&A, 432, 369
Schuller, F., Menten, K. M., Contreras, Y., et al. 2009, A&A, 504, 415
Sellgren, K. 1986, ApJ, 305, 399
Smith, R. J., Glover, S. C. O., Clark, P. C., Klessen, R. S., & Springel, V. 2014, MNRAS, 441, 1628
Snow, T. P. & McCall, B. J. 2006, ARA&A, 44, 367
Stanimirović, S., Weisberg, J. M., Dickey, J. M., et al. 2003, ApJ, 592, 953
Sternberg, A. 1989a, in Infrared Spectroscopy in Astronomy, ed. E. Böhm-Vitense, 269
Sternberg, A. 1989b, ApJ, 347, 863
Turner, B. E. 1966, Nature, 212, 184
Turner, B. E. & Heiles, C. 1971, ApJ, 170, 453
Umemoto, T., Minamidani, T., Kuno, N., et al. 2017, PASJ, 69, 78
van Dishoeck, E. F. & Black, J. H. 1988, ApJ, 334, 771
van Dishoeck, E. F., Herbst, E., & Neufeld, D. A. 2013, Chemical Reviews, 113, 9043
Wampfler, S. F., Bruderer, S., Karska, A., et al. 2013, A&A, 552, A56
Wampfler, S. F., Bruderer, S., Kristensen, L. E., et al. 2011, A&A, 531, L16
Wang, Y., Beuther, H., Rugel, M. R., et al. 2020, A&A, 634, A83
Wang, Y., Bihr, S., Rugel, M., et al. 2018, A&A, 619, A124
Weselak, T., Galazutdinov, G. A., Beletsky, Y., & Krełowski, J. 2010, MNRAS, 402, 1991
Wiesemeyer, H., Güsten, R., Heyminck, S., et al. 2016, A&A, 585, A76
Wiesemeyer, H., Güsten, R., Heyminck, S., et al. 2012, A&A, 542, L7
Wilson, R. W., Jefferts, K. B., & Penzias, A. A. 1970, ApJ, 161, L43
Witt, A. N., Stecher, T. P., Boroson, T. A., & Bohlin, R. C. 1989, ApJ, 336, L21
Wolfire, M. G., Hollenbach, D., & McKee, C. F. 2010, ApJ, 716, 1191
Xu, D., Li, D., Yue, N., & Goldsmith, P. F. 2016, ApJ, 819, 22
York, D. 1966, Canadian Journal of Physics, 44, 1079
Young, E. T., Becklin, E. E., Marcum, P. M., et al. 2012, ApJ, 749, L17
Zhang, B., Moscadelli, L., Sato, M., et al. 2014, ApJ, 781, 89

Appendix A: Additional spectra and results

Appendix B: Overview SOFIA data

Appendix A: Additional spectra and results

Table A.1. OH, HI, and CO column densities

Source	v_{mid} [km s^{-1}]	R_{GC} [kpc]	OH 1667 MHz $\int\tau dv$ [km s^{-1}]	τ_{max}	OH 1665 MHz $\int\tau dv$ [km s^{-1}]	τ_{max}	OH 1612 MHz $\int\tau dv$ [km s^{-1}]	τ_{max}	OH 1720 MHz $\int\tau dv$ [km s^{-1}]	τ_{max}	HI $\int\tau dv$ [km s^{-1}]	τ_{max}	$\frac{N_{OH}}{T_{ex}}$ [$\times10^{13}\frac{cm^{-2}}{K}$]	$\frac{N_{HI}}{T_S}$ [$\times10^{19}\frac{cm^{-2}}{K}$]	^{12}CO $J{=}1{-}0$ $\int T_{mb}dv$ [K km s^{-1}]	^{13}CO $J{=}1{-}0$ $\int T_{mb}dv$ [K km s^{-1}]	C^{18}O $J{=}1{-}0$ $\int T_{mb}dv$ [K km s^{-1}]	^{13}CO $J{=}1{-}0$ $\int T_{mb}dv$ [K km s^{-1}]	N_{H_2} [$\times10^{20}$ cm^{-2}]
G21.347−0.629	+7.4	7.64	+0.25	+0.14	+0.14	+0.07	<0.07	<0.01	+0.03	+0.02	>18.95	>3.66			24.5	1.5	<1.3	1.5	49.0
	+51.6	5.07	+0.36	+0.14	+0.17	+0.07	+0.00	+0.01	+0.06	+0.04	>10.82	>3.64	8.09	>1.97	51.9	11.5	<1.3	11.5	103.7
	+56.5	4.87	+0.50	+0.37	+0.32	+0.28	-0.04	+0.00	+0.15	+0.13	>9.04	>3.70	11.17	>1.65	22.2	9.7	2.9	9.7	44.5
	+73.5	4.24	+0.13	+0.04	+0.06	+0.03	+0.04	+0.02	<0.06	<0.01	+7.31	+1.38	2.86	1.33	16.1	<1.3	<1.3	<1.3	32.1
	+68.8	4.41	+0.05	+0.06	+0.02	+0.03	<0.02	<0.01	<0.02	<0.01	+0.58	+0.36	1.13	0.11	<2.4	<1.3	<1.3	<1.3	<4.9
	+66.6	4.48	+0.05	+0.05	+0.03	+0.03	<0.02	<0.01	<0.02	<0.01	+0.50	+0.27	1.07	0.09	2.2	<1.3	<1.3	<1.3	4.4
G29.957−0.018	+6.5	7.87	+0.19	+0.12	+0.11	+0.07	+0.08	+0.06	-0.03	+0.01	+4.19	+1.56	4.27	0.76	12.9	2.2	<1.3	2.2	25.8
	+9.7	7.68	+0.08	+0.07	+0.05	+0.04	+0.04	+0.03	<0.02	<0.01	+2.67	+1.14	1.84	0.49	2.6	<1.3	<1.3	<1.3	5.1
	+67.5	5.18	+0.10	+0.03	+0.05	+0.02	+0.04	+0.02	<0.06	<0.01	+7.55	+1.26	2.15	1.38	21.9	4.3	<1.3	4.3	43.8
	+97.8	4.32	+0.14	+0.06	+0.09	+0.04	-0.03	+0.02	+0.08	+0.06	+13.24	>3.59	3.18	>2.41	160.6	63.9	13.9	63.9	321.1*
	+102.8	4.19	+0.14	+0.06	-0.25	+0.01	-0.19	+0.00	+0.16	+0.07	+12.18	>3.59	3.21	>2.22	87.1	24.6	4.4	24.6	174.1*

For the two sources below, the ^{12}CO, ^{13}CO and C^{18}O columns refer to the $J{=}2{-}1$ transition; the final CO column is ^{13}CO $J{=}1{-}0$.

Source	v_{mid} [km s^{-1}]	R_{GC} [kpc]	OH 1667 MHz $\int\tau dv$ [km s^{-1}]	τ_{max}	OH 1665 MHz $\int\tau dv$ [km s^{-1}]	τ_{max}	OH 1612 MHz $\int\tau dv$ [km s^{-1}]	τ_{max}	OH 1720 MHz $\int\tau dv$ [km s^{-1}]	τ_{max}	HI $\int\tau dv$ [km s^{-1}]	τ_{max}	$\frac{N_{OH}}{T_{ex}}$ [$\times10^{13}\frac{cm^{-2}}{K}$]	$\frac{N_{HI}}{T_S}$ [$\times10^{19}\frac{cm^{-2}}{K}$]	^{12}CO $J{=}2{-}1$ $\int T_{mb}dv$ [K km s^{-1}]	^{13}CO $J{=}2{-}1$ $\int T_{mb}dv$ [K km s^{-1}]	C^{18}O $J{=}2{-}1$ $\int T_{mb}dv$ [K km s^{-1}]	^{13}CO $J{=}1{-}0$ $\int T_{mb}dv$ [K km s^{-1}]	N_{H_2} [$\times10^{20}$ cm^{-2}]
G29.935−0.053	+7.5	7.81	+0.15	+0.07	+0.09	+0.05	+0.08	+0.05	<0.12	<0.04	+5.53	+1.29	3.47	1.01	3.4	0.4	<0.2	<1.3	9.8
	+50.8	5.77	+0.29	+0.14	+0.13	+0.06	<0.12	<0.04	<0.11	<0.04	>11.84	>2.64	6.39	>2.16	22.5	5.6	0.8	7.8	64.3
	+68.0	5.17	+0.20	+0.14	+0.13	+0.09	+0.09	+0.05	<0.08	<0.04	>8.30	>2.62	4.56	>1.51	9.9	1.1	<0.2	3.2	28.4
	+99.0	4.29	+0.76	+0.26	+0.64	+0.18	-0.07	+0.03	+0.27	+0.08	>18.10	>2.64	17.07	>3.30	113.7	58.1	18.2	72.3	377.5^{a},*
G31.388−0.383	-3.8	8.54	+0.10	+0.07	+0.04	+0.03	+0.03	+0.02	<0.03	<0.02	+1.16	+0.57	2.27	0.21	1.5	0.2	<0.2	<0.9	4.3
	+18.0	7.25	+0.22	+0.14	+0.11	+0.08	+0.04	+0.03	+0.02	+0.02	+22.74	>3.89	4.98	>4.14	7.6	0.6	<0.2	<0.9	21.8
	+37.0	6.38	+0.03	+0.04	<0.03	<0.02	<0.03	<0.02	<0.03	<0.02	+2.15	+0.88	0.74	0.39	0.3	<0.2	<0.2	<0.9	0.8
	+73.1	5.11	+0.12	+0.04	+0.06	+0.03	+0.07	+0.02	-0.06	+0.00	+17.18	+3.59	2.58	3.13	7.3	0.5	<0.2	2.5	20.9
	+78.1	4.96	+0.12	+0.12	+0.07	+0.07	+0.03	+0.02	+0.01	+0.02	+5.67	+2.39	2.64	1.03	2.0	0.2	<0.2	0.7	5.8
	+81.8	4.85	+0.06	+0.04	<0.03	<0.02	<0.03	<0.02	<0.03	<0.02	>11.84	>3.85	1.37	>2.16	3.6	0.4	<0.2	1.0	10.4
	+85.3	4.75	+0.11	+0.07	+0.03	+0.03	<0.03	<0.02	<0.03	+0.02	>13.04	>3.87	2.53	>2.38	2.8	0.2	<0.2	0.4	7.9
	+92.0	4.57	+0.05	+0.04	+0.04	+0.02	<0.03	<0.01	<0.03	<0.02	+6.65	+2.47	1.19	1.21	4.7	0.5	<0.2	1.5	13.4

Notes. Integral and peak of the optical depth of the OH and H I lines, as well as of CO emission in specific velocity intervals with the mid-point of each chosen velocity range tabulated in column 1. The CO isotopologue and transition reported here and used to determine the H$_2$ column density is indicated in brackets in the last column. As we do not derive the excitation temperatures of the OH and H I lines in this work, we report N_{OH}/T_{ex} and N_{HI}/T_S. (*) Features associated with H II regions. All other features are line-of-sight absorption features. (^{a}) Using ^{13}CO $J = 1 - 0$ and correcting for isotope ratio variations over Galactocentric distance (Sect. 3.2).
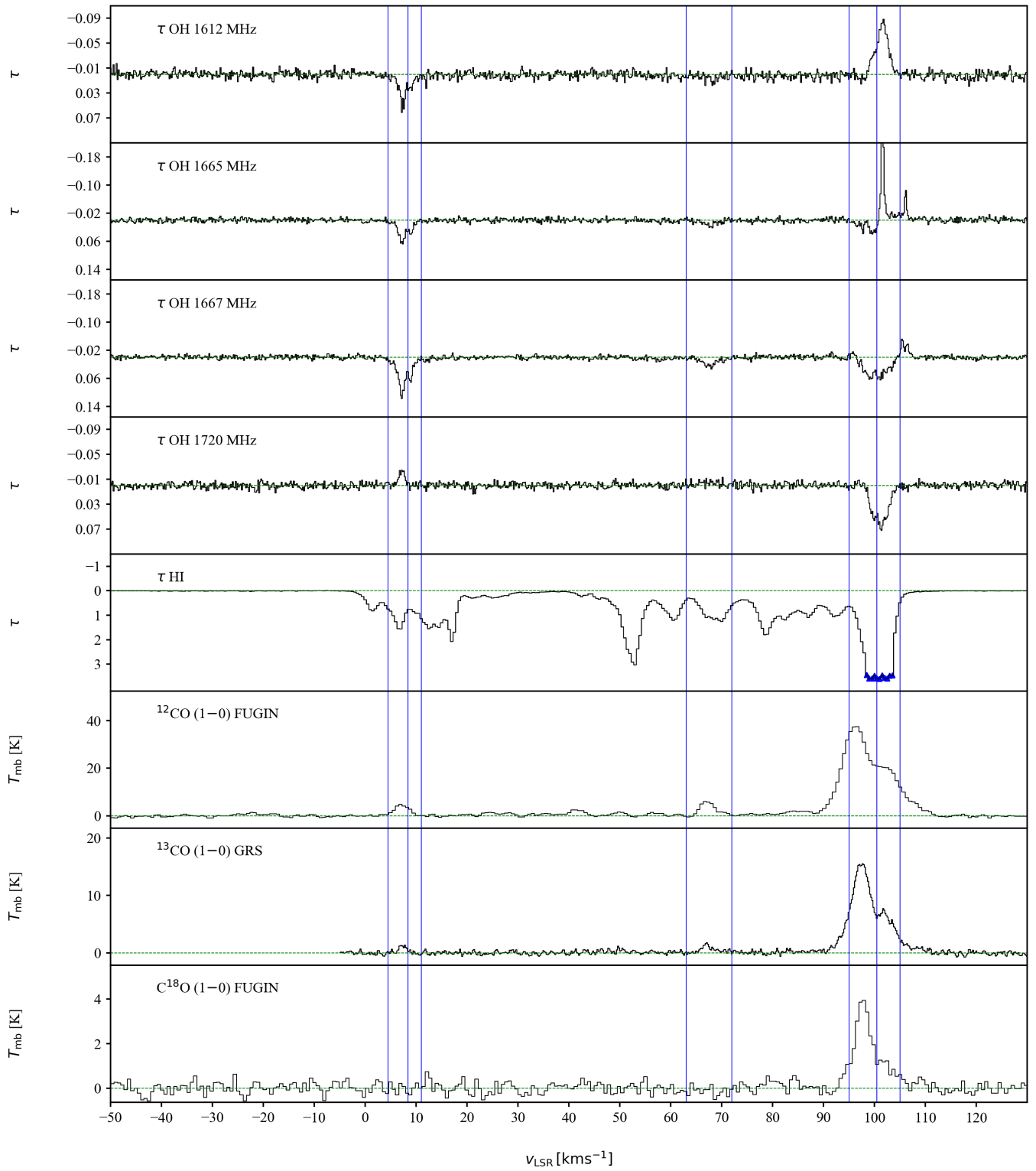
G21.347−0.629
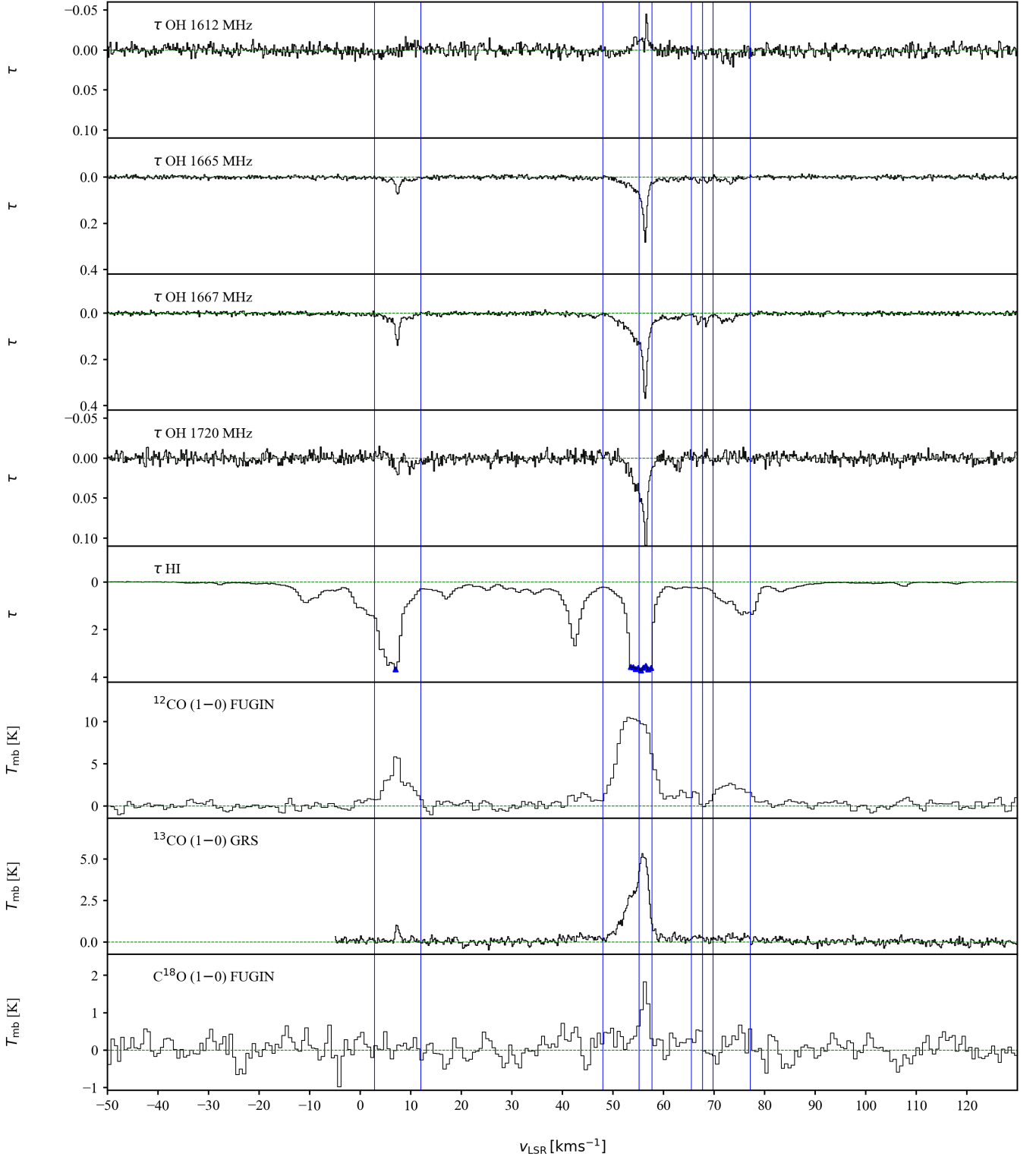
Fig. A.1. Same as Fig. 2, but towards G21.347−0.629, except the CO data presented is taken from FUGIN (Umemoto et al. 2017) and GRS (Jackson et al. 2006) surveys. No [C II] 158 μm emission spectrum has been recorded for this source.
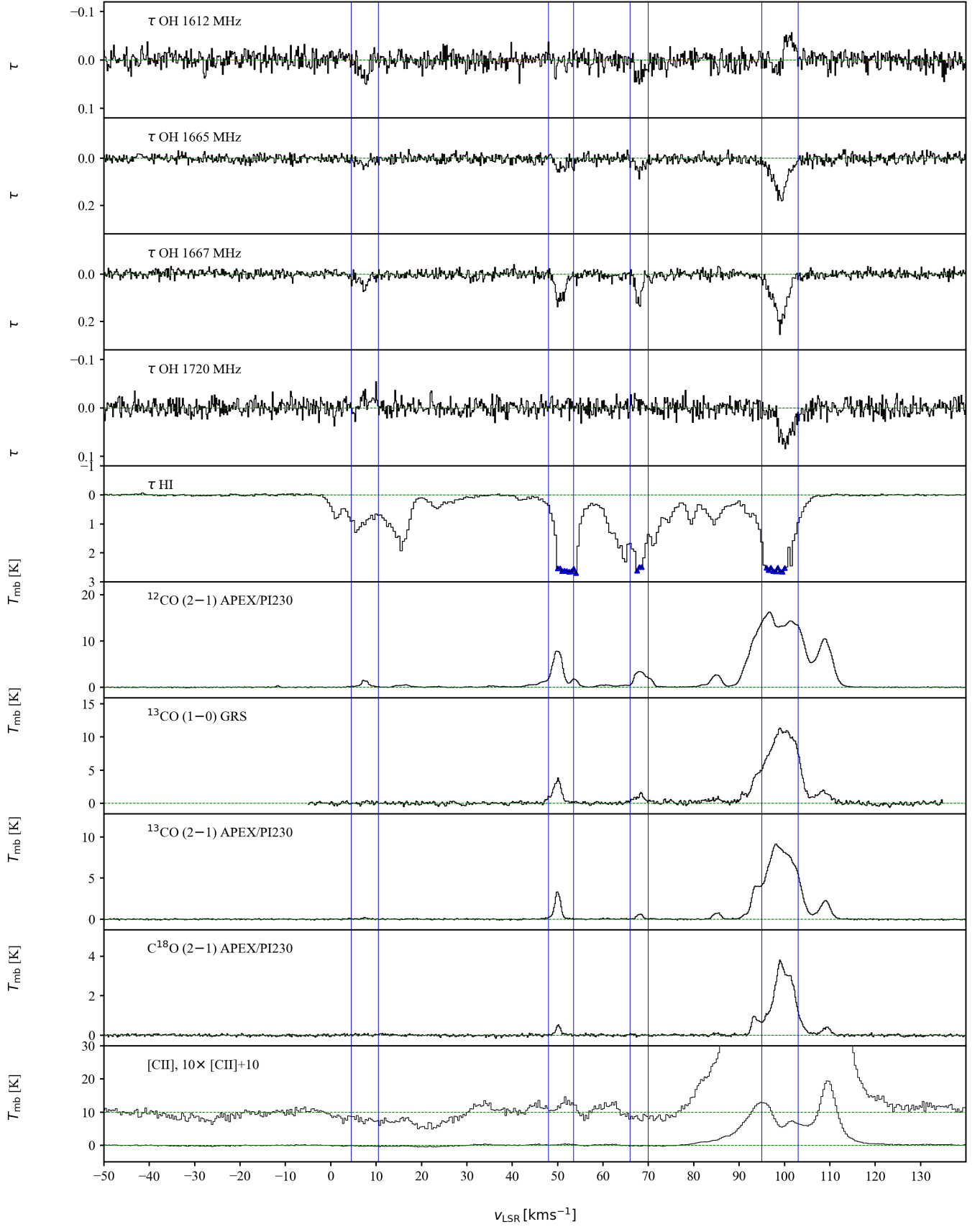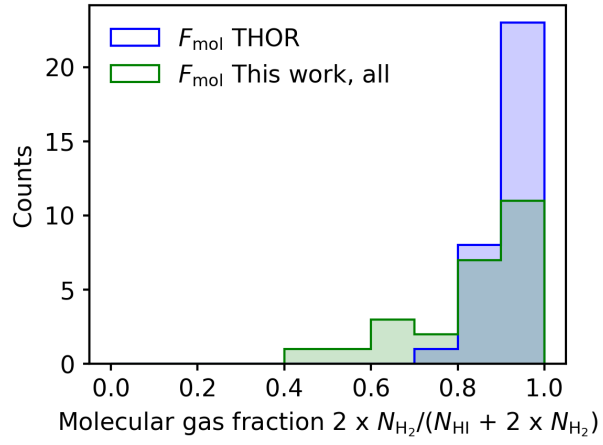
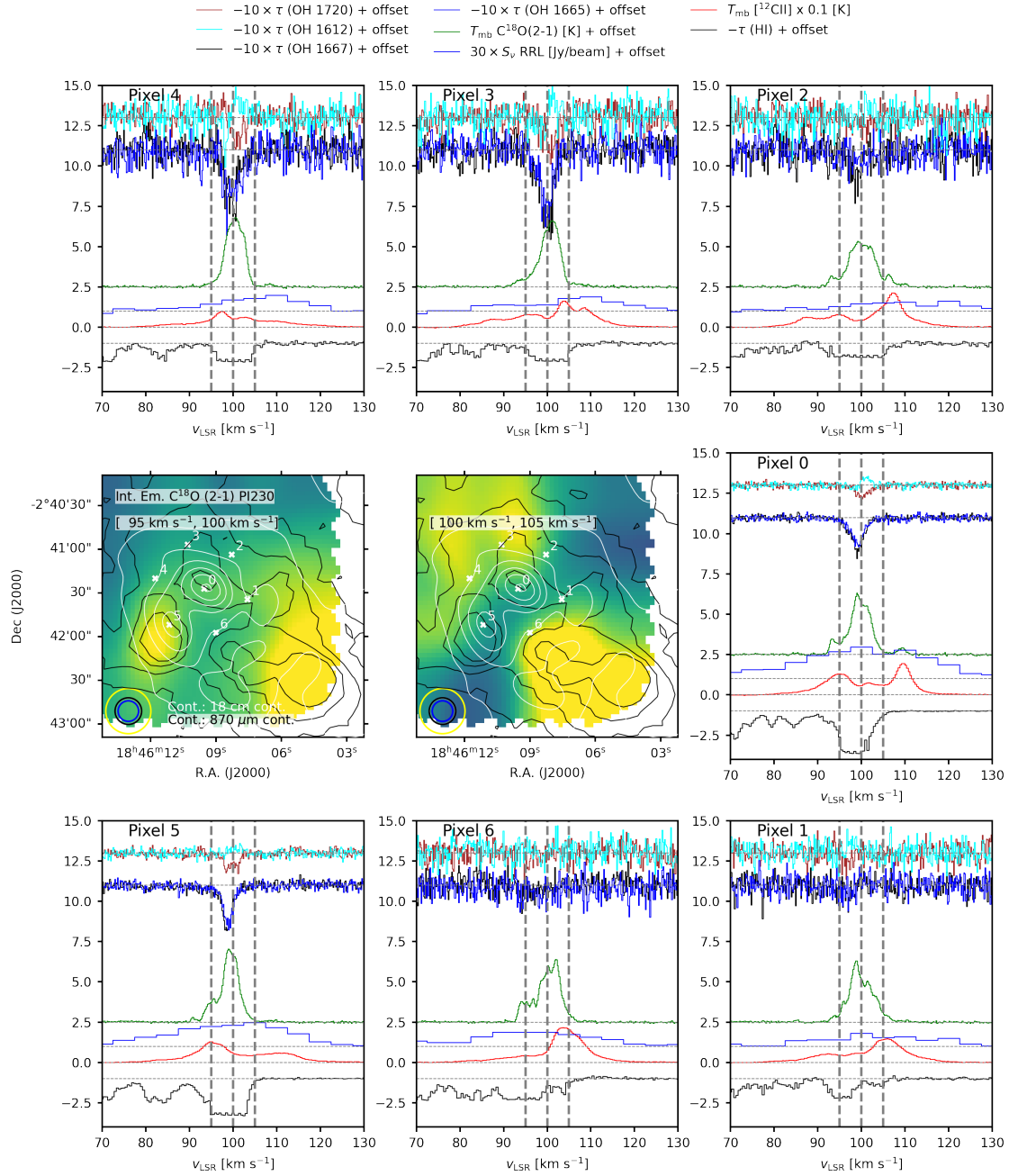G29.957−0.018

Fig. A.2. Same as Fig. A.1, but for G29.957−0.018

G29.935−0.053

Fig. A.3. Same as Fig. 2, but for G29.935−0.053. The bottom panel includes an enlarged view of the [C ɪɪ] 158 μm line for better visibility of the faint emission or absorption components, and/or baseline ripples.

Fig. A.4. As Fig. 5, but for $T_{spin} = 50$ K.

Fig. A.5. Optical depth of the OH lines at 1612 MHz, 1665 MHz, 1667 MHz and 1720 MHz, as well of H I towards the seven pixels towards G29.935−0.053 of the upGREAT/SOFIA [^{12}C II] observations, as well as accompanying C^{18}O (2–1) (APEX/PI230) and stacked radio recombination lines (40″, GLOSTAR; Brunthaler et al. 2021; Khan et al. 2024). The maps in the middle panel are repeated for clarity from row 2 in Fig. 7.
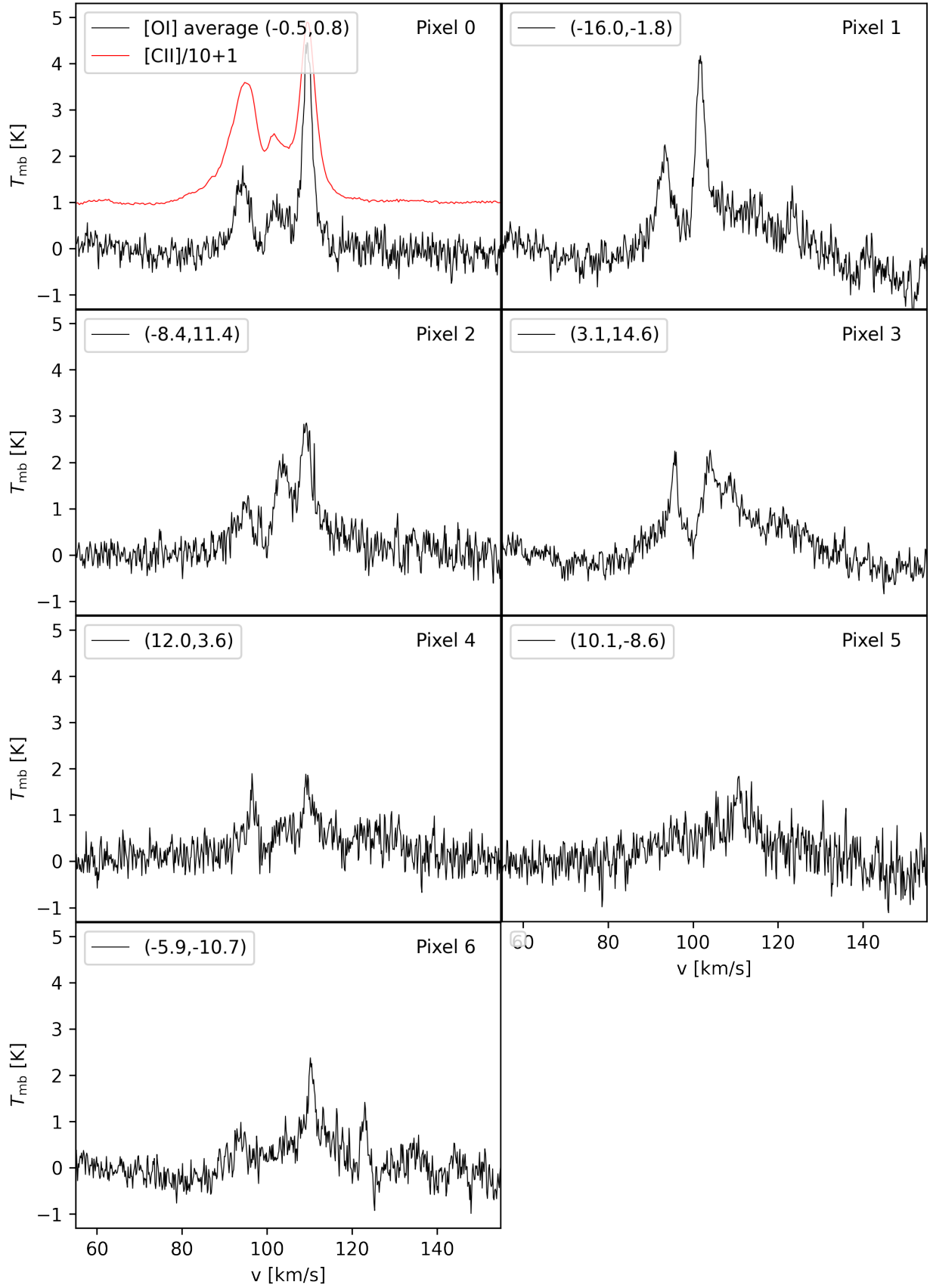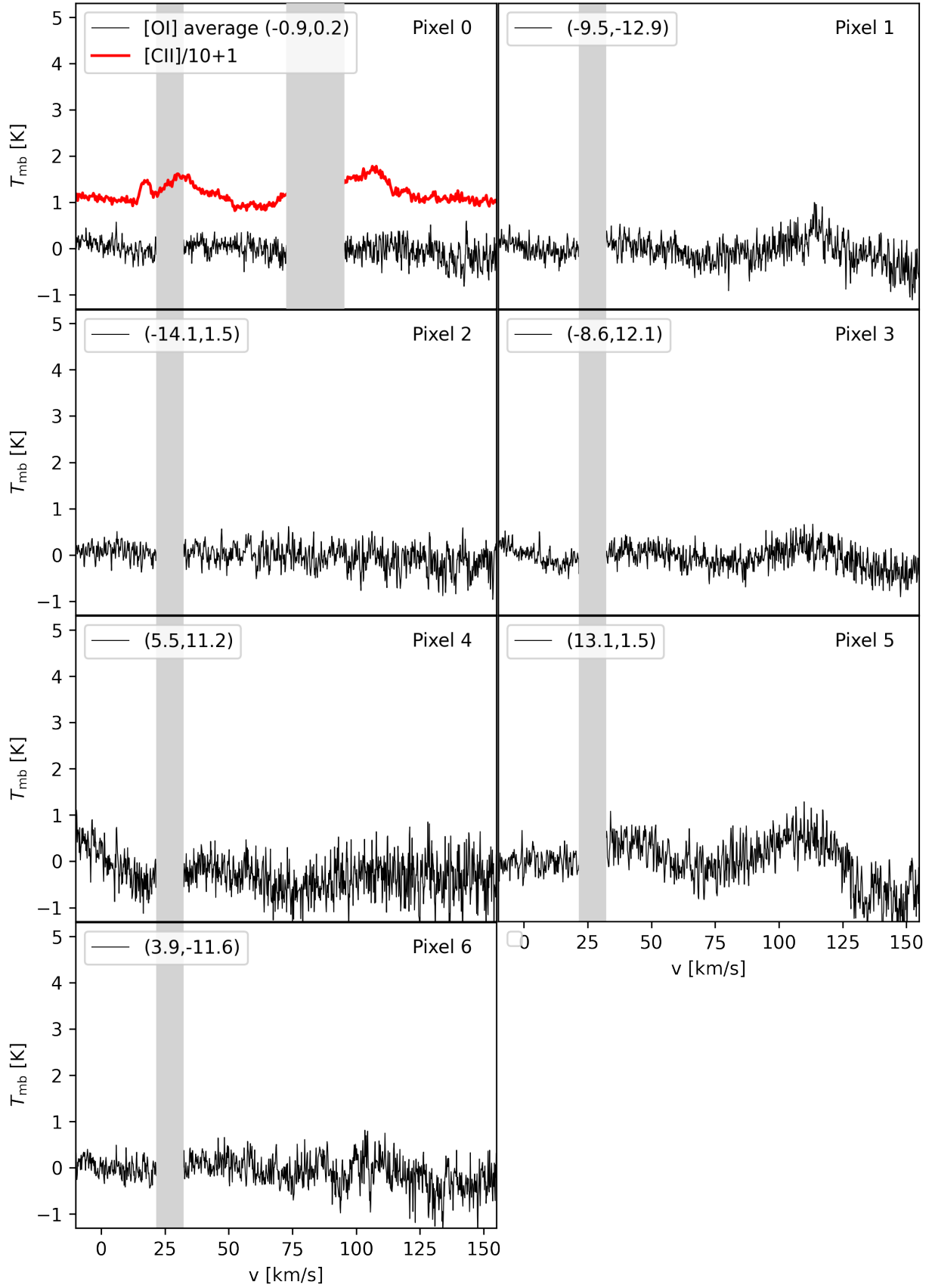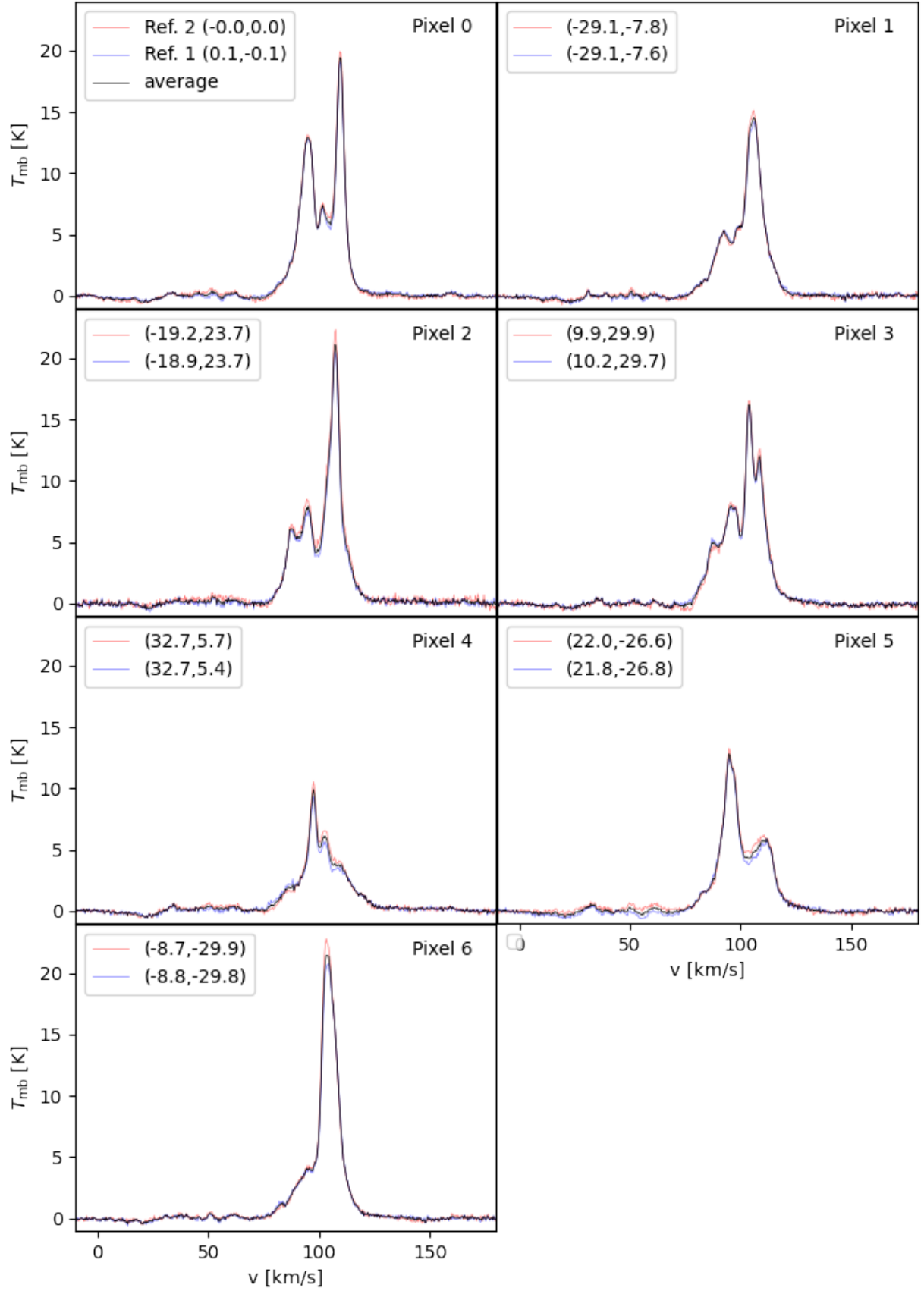
Fig. B.1. [O I] 63 μm emission towards G29.935−0.053. For each spectrum, we show the average of all data (*black*). We only show the [C II] 158 μm emission for reference in pixel 1, as the other pixels are closer to the central beam than for [C II] 158 μm and do not overlap. Offsets from the source position are indicated in arcsec.
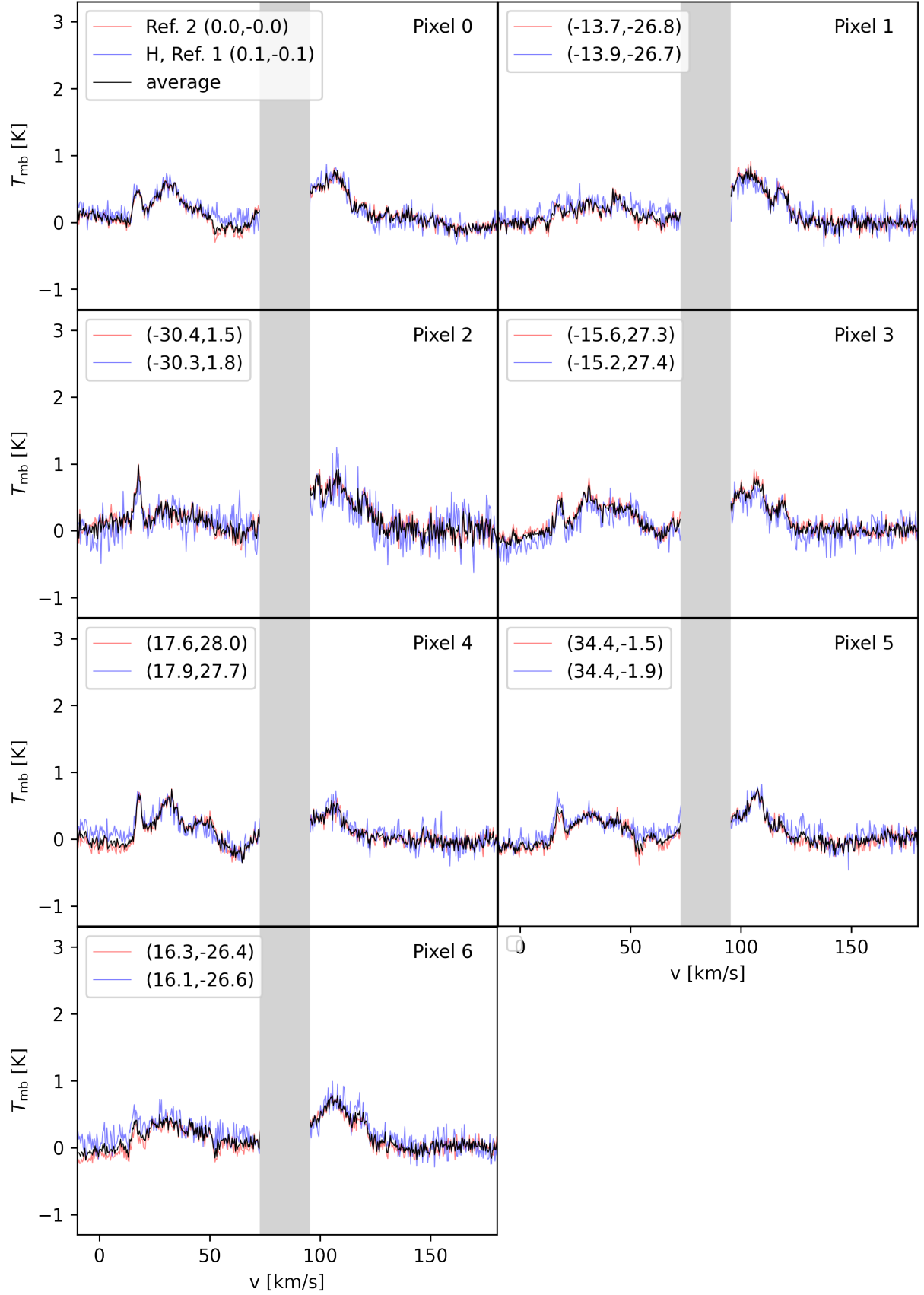
Fig. B.2. [C II] 158 μm emission towards G31.388−0.383. For each spectrum, we show the average of all data (*black*), as well as averages by polarization and by reference position. Note that only vertical polarization ("V") is available for Pixel 2. The gray-shaded region is masked as it is contaminated by emission in the reference position.

Fig. B.3. [O I] 63 μm emission towards G31.388−0.383. For each spectrum, we show the average of all data (*black*). We only show the [C II] 158 μm emission for reference in pixel 1, as the other pixels are closer to the central beam than for [C II] 158 μm and do not overlap. Several pixels show residual low-frequency baseline ripples. The gray-shaded region around 25 km s^{-1} is masked due to residual artefacts from atmospheric corrections.
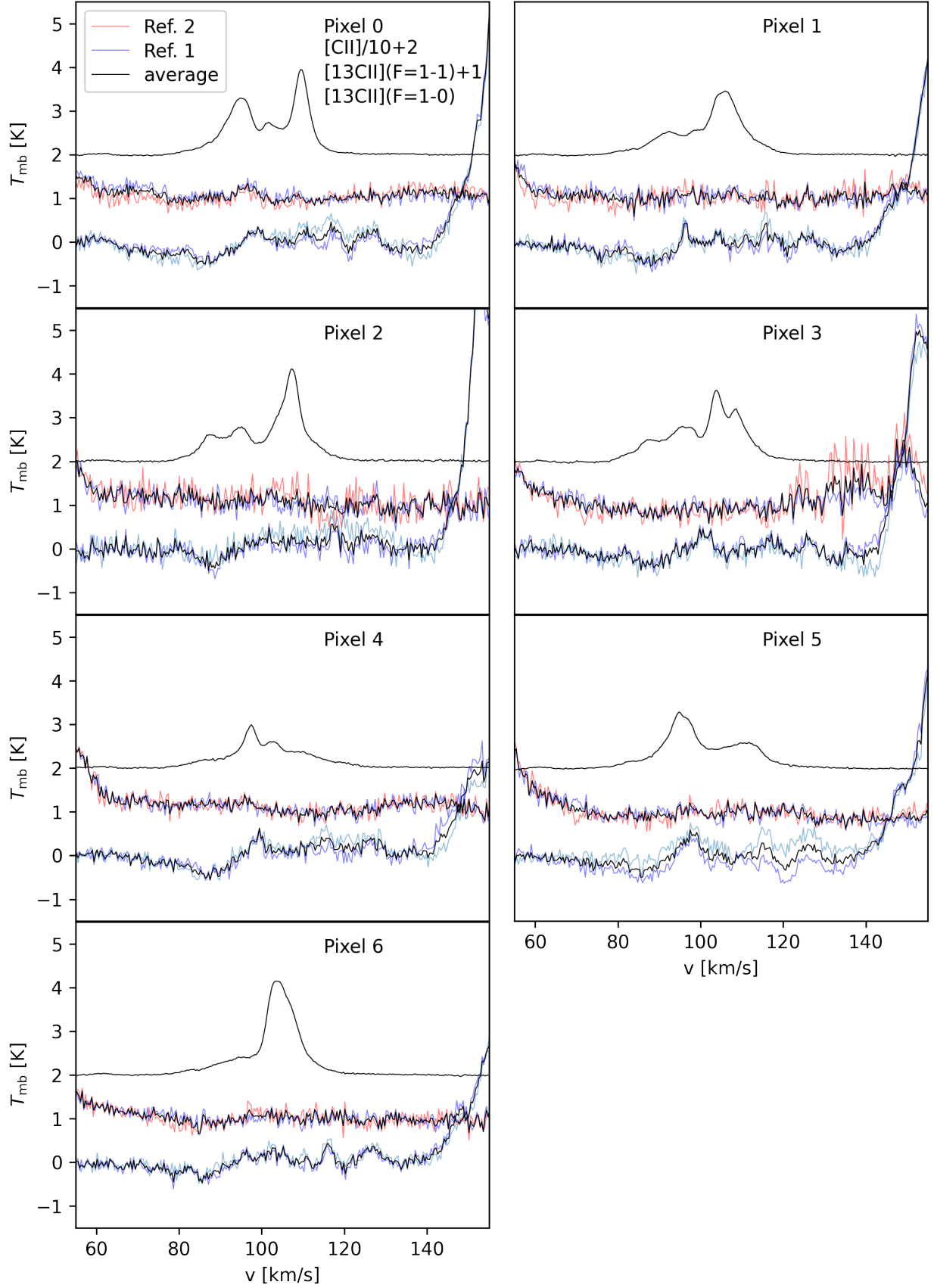
Fig. B.4. [C II] 158 μm emission towards G29.935−0.053. For each spectrum, we show the average of all data (*black*), as well as averages by reference position. Note that only vertical polarization ("V") is available for Pixel 2. The pixel offset from the "H"The gray-shaded region is masked as it is contaminated by emission in the reference position.
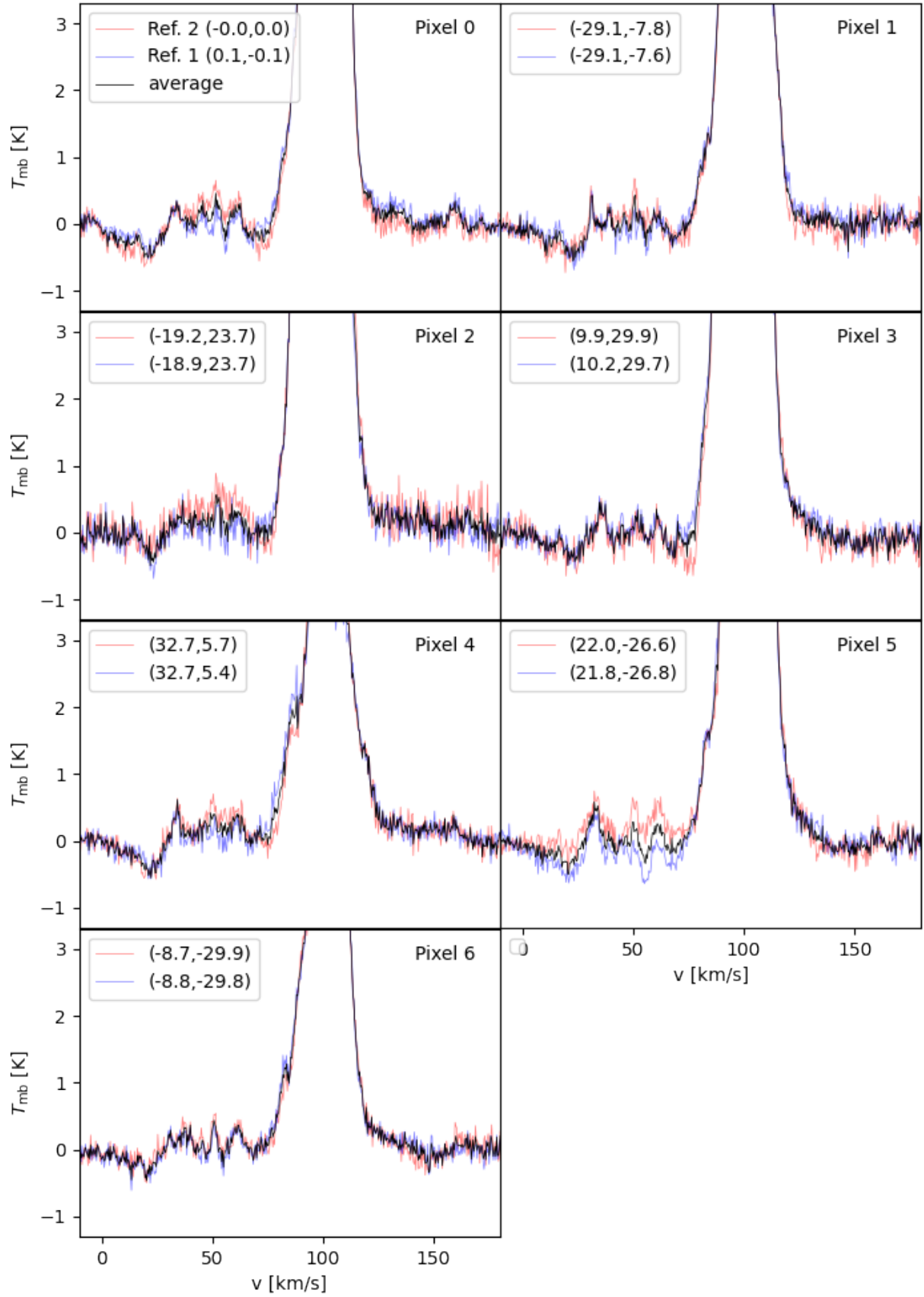
Fig. B.5. Zoom-in on the low-level [C II] 158 μm emission in G29.935−0.053. Colors and spectra as in Fig. B.4.

Fig. B.6. [C II] 158 μm and [^{13}C II] emission towards G29.935−0.053. Colors and spectra as in Fig. B.4, with the spectra in each subplot shifted to the rest frequency of each line.